Missouri S&T Library and Learning Resources

Scholars' Mine

Masters Theses | Student Theses and Dissertations

Fall 2018

Spatial resolution study for magnetic near-field probe

Xin Yan

Follow this and additional works at: https://scholarsmine.mst.edu/masters_theses

Part of the Electrical and Computer Engineering Commons

Department:

Recommended Citation

Yan, Xin, "Spatial resolution study for magnetic near-field probe" (2018). *Masters Theses*. 7843.
https://scholarsmine.mst.edu/masters_theses/7843

This thesis is brought to you by Scholars' Mine, a service of the Missouri S&T Library and Learning Resources. This work is protected by U. S. Copyright Law. Unauthorized use including reproduction for redistribution requires the permission of the copyright holder. For more information, please contact scholarsmine@mst.edu.

SPATIAL RESOLUTION STUDY FOR MAGNETIC NEAR-FIELD PROBE

by

XIN YAN

A THESIS

Presented to the Faculty of the Graduate School of the

MISSOURI UNIVERSITY OF SCIENCE AND TECHNOLOGY

In Partial Fulfillment of the Requirements for the Degree

MASTER OF SCIENCE IN MECHANICAL ENGINEERING

2018

Approved by:

Dr. Jun Fan, Advisor
Dr. David J. Pommerenke
Dr. Victor Khilkevich

© 2018

Xin Yan

All Rights Reserved

PUBLICATION THESIS OPTION

This thesis consists of the following paper which has been published as follows:

Paper I: Pages 36-50 have been published in 2018 IEEE Symposium on Electromagnetic Compatibility, Signal Integrity and Power Integrity (EMC, SI & PI).

ABSTRACT

Spatial resolution is an important factor of near-field probe, which represents the ability to distinguish two close radiation sources. Traditional definition of spatial resolution is the distance between peak point and -6dB point when measuring microstrip line. The definition has disadvantage and limitation. In this topic, spatial resolution for magnetic near-field probe is studied, and three dimensions of spatial resolution are put forward. An optimized measurement setup is presented to reflect spatial resolution of probe properly. Then, an example is given to show how spatial resolution affects field distribution in near-field measurement.

ACKNOWLEDGMENTS

I would like to express my sincere gratitude to my advisor, Dr. Jun Fan, for the support and guidance in my research work. He is a very supportive person and would listen and help me whenever I would come with difficulties. Also, I want to thank Dr. David Pommerenke and Dr. Chulsoon Hwang for helping me in research.

I want to thank Jianchi Zhou for accompanying me in these years. We have shared happiness and experiences. We encourage each other when struggling with something, both in research and life. There have been lots of wonderful memories. Besides, I want to thank all the members of the “Electromagnetic Compatibility Laboratory” at Missouri University of Science and Technology for all their support and encouragement.

TABLE OF CONTENTS

Page

PUBLICATION THESIS OPTION iii

ABSTRACT iv

ACKNOWLEDGMENTS v

LIST OF ILLUSTRATIONS viii

LIST OF TABLES xi

SECTION

1. INTRODUCTION 1

2. OVERVIEW 2

3. SPATIAL RESOLUTION ANALYSIS 7

3.1. FIRST DIMENSION OF SPATIAL RESOLUTION 7

3.1.1. Microstrip Model 7

3.1.2. Probe Model. 12

3.2. SECOND DIMENSION OF SPATIAL RESOLUTION 14

3.3. THIRD DIMENSION OF SPATIAL RESOLUTION 16

4. OPTIMIZED MEASUREMENT SETUP OF SPATIAL RESOLUTION 26

5. EFFECT OF SPATIAL RESOLUTION IN NEAR-FIELD MEASUREMENT 31

6. SUMMARY 34

PAPER

I. A 20GHZ LANDING PROBE DESIGN BASED ON POGO-PINS 36

ABSTRACT 36

1. INTRODUCTION 37

2. DESIGN OF THE LANDING PROBE 39

2.1. POGO-PIN 39

2.2. PROBE 40

2.3. LANDING PROBE 41

3. MEASUREMENT VALIDATION 43

4. CONCLUSION 47

ACKNOWLEDGMENTS 48

REFERENCES 49

SECTION

7. CONCLUSION 51

REFERENCES 52

VITA 54

LIST OF ILLUSTRATIONS

Figure Page

SECTION

2.1 Hx field distribution along x-axis direction above microstrip 2

2.2 Hx field distribution above much wider microstrip 3

2.3 Improve the spatial resolution with offset measurement 4

2.4 Structure of space different probe which can improve spatial resolution 5

3.1 (a) 3D model of microstrip line (b) cross-section view 8

3.2 (a) S11 (b) S21 of microstrip strip 8

3.3 Numerical model of microstrip 9

3.4 Comparison between analytical and simulation model 10

3.5 Schematic of analytical probe model 10

3.6 Comparison of voltage distribution between (a) different loop width and (b) different loop height 11

3.7 (a) Probe tip structure (b) stack-up information 12

3.8 (a) HFSS model (b) frequency response of probe 13

3.9 Comparison of simulation results between different loop width 13

3.10 Numerical model after rotating 45 degrees 14

3.11 Comparison of analytical results between different loop width 15

3.12 Comparison of simulation results between different loop width 15

3.13 Diagram of electrical center and geometrical center 17

3.14 Tangential H-field strength across the trace at different heights 17

3.15 (a) Modified probe (b) frequency response 18

3.16 Tangential H-field strength measured by probe and original field 19

3.17 Schematic of approximate voltage calculation 20

3.18 Smoothing on one-dimensional array 21

3.19 Analytical model of two turns loop 22

3.20 Comparison of analytical results between one turn and two turn loops 23

3.21 Structure of two turn loops in simulation model 24

3.22 Voltage distribution simulated by 1 turn and 2 turns probe.................................... 24

3.23 Structure of modified wider probe 25

3.24 (a) Simulated voltage distribution of 1 turn and 2 turns probe (b) results comparison between 1 turn and 1 turn thicker probe... 25

4.1 Bend microstrip model.. 26

4.2 Hx field distribution along x-axis (a) and y-axis (b)... 27

4.3 Hx-field distribution along y-axis 28

4.4 Simulation model of bend microstrip and probe... 29

4.5 Hx-field distribution along y-axis 29

5.1 Part of a board model with 4 resistors 31

5.2 Scan area in simulated near-field measurement.. 32

5.3 Simulated field distribution by different probes 32

6.1 Three dimensions of spatial resolution 34

PAPER I

1 (a) Specification of a pogo-pin [13] (b) simplified 3D model of a pogo-pin (c) cross-sectional view of a pogo-pin [14] 39

2 (a) Dimensions of the probe with pogo-pins (b) and stack-up information................. 40

3 A landing pad is added at the landing position 42

4 (a) Fabricated Probe and (b) landing board 43

5 Measurement setup 43

6 Simulation vs. Measurement results 44

7 Measurement results with different pad diameters 44

8 TDR results 45

LIST OF TABLES

Table Page

SECTION

3.1 Original one-dimensional array 20

3.2 New one-dimensional array after smoothing 21

1. INTRODUCTION

Recent modern digital and radio frequency systems evolve toward the direction of high integration, high performance, and compact size. However, High-speed digital circuits can generate high frequency noise due to their switching nature, and PCB designs are more and more vulnerable to signal integrity (SI) and electromagnetic compatibility (EMC) issues [1]-[3]. Near-field measurement is an effective method to locate radiation source, where near-field probes are usually used for near-field pattern acquisition over PCB, which in turn provides insights of trace routing, layout, component radiation properties etc. Based on measured near-field pattern, radiation source or ground current reconstruction have been widely studied [4]-[6]. Spatial resolution and sensitivity are two important factors for field probes. Besides field probe, the landing probe is generally employed for S-parameter and TDR measurement [7], [8]. The DUT for the landing probe is usually narrow traces.

In first section, spatial resolution for magnetic near-field probe is studied, and three dimensions of spatial resolution are put forward. An optimized measurement setup is presented, which can reflect spatial resolution of probe properly. Then, an actual board is used to show the effect of spatial resolution in near-field measurement. In second section, a landing probe design is proposed in this paper based on pogo-pins. The designed probe works well up to 20 GHz, which is validated by measurement.

2. OVERVIEW

Sensitivity and spatial resolution are two important factors of magnetic near-field probe. Sensitivity describes the ability to detect weak radiation source. Sensitivity improvement has been widely studied: use resonant structure to increase sensitivity at certain frequencies [9][10], or minimize the loss and use ultra low-noise amplifier to increase Signal to Noise ratio [11][12]. Spatial resolution represents the ability to distinguish two close radiation sources. However, spatial resolution is a special factor, as it depends not only on probe but also on DUT [13]. A common method to define spatial resolution 'good' or 'bad' is to measure output distribution over a microstrip line. A typical field distribution above the microstrip is shown in Figure 2.1.

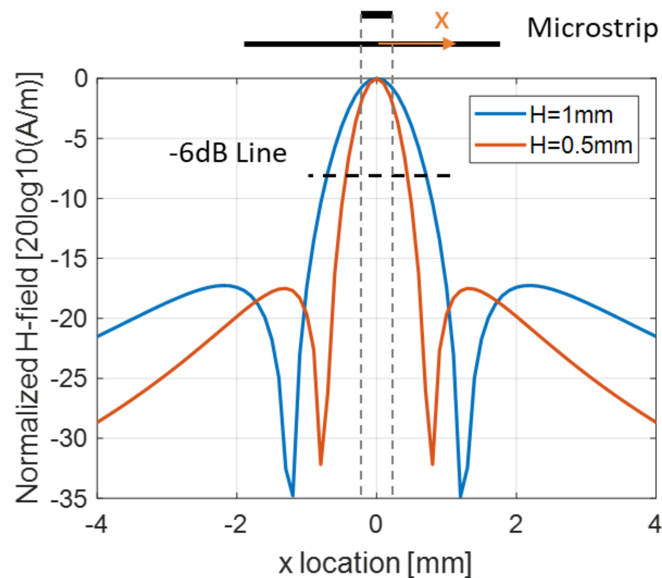

Figure 2.1 Hx field distribution along x-axis direction above microstrip

In Figure 2.1, blue curve is Hx-field above microstrip 1mm, and red curve is the field above 0.5mm. Field strength is already normalized. Field distribution measured by a

magnetic probe which is able to detect horizontal field has similar shape as above curves. Typically, spatial resolution is defined as the distance between peak point and -6dB point [13]-[19]. This definition is straight forward. If the difference of field strength is less than 6dB in a small area, than it can be assumed that there is only one radiation source, or multiple sources are not able to be distinguished. The distance between peak point and -6dB point decreases with measurement height decreasing, so reduce measurement height is a good way to increase spatial resolution without redesigning near-field probe. Also, there are two dips of field distribution at both side of microstrip, and the distance between two dips decreases with measurement height reducing, which means this distance can also reflect spatial resolution. When resolution of different probe is measured, DUT and measurement height need to be fixed to make sure the values of spatial resolution are comparable.

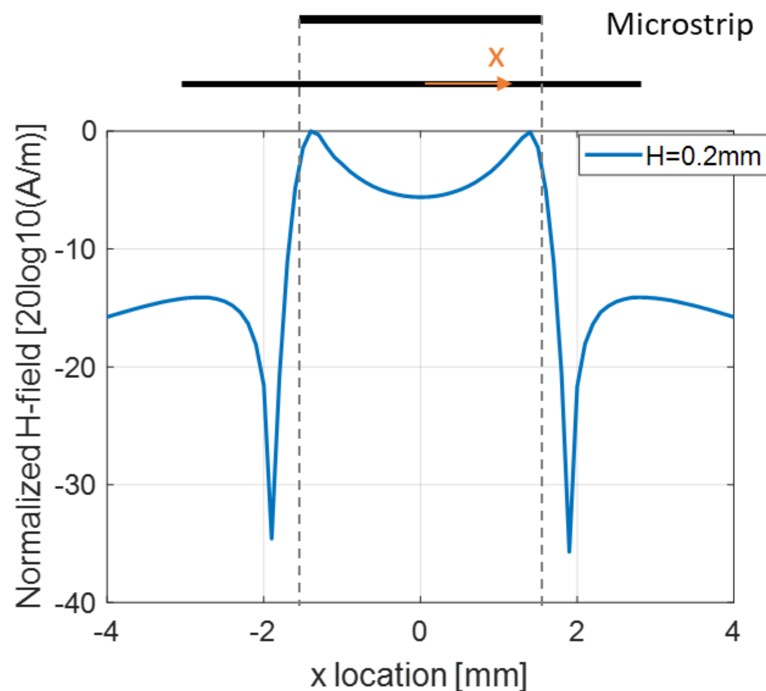

Figure 2.2 Hx field distribution above much wider microstrip

Another way to compare the spatial resolution between different probes is that using much wider microstrip, which is proposed in [13]. When high-frequency current is flowing through a microstrip line, considering skin effect, the current density is concentrated on both edges of microstrip. Simulated field distribution above wide microstrip is shown in Figure 2.2.

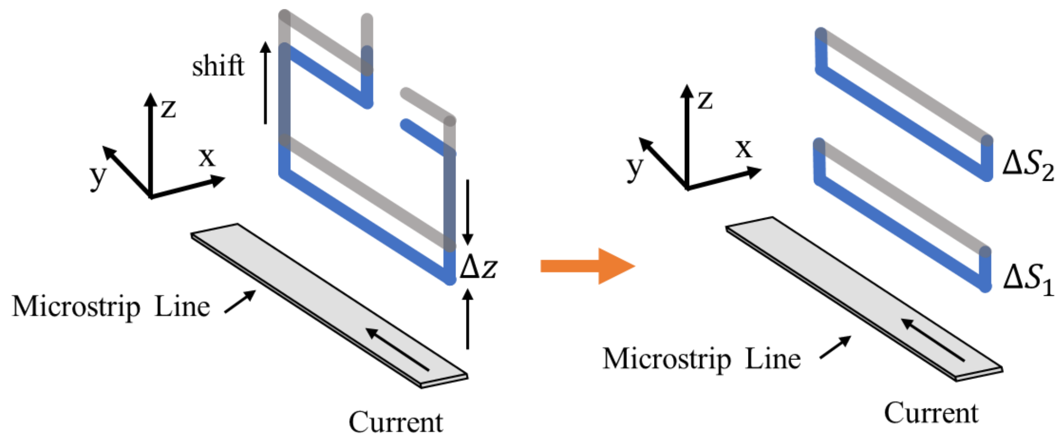

Figure 2.3 Improve the spatial resolution with offset measurement

A simplest method to design a magnetic probe with high spatial resolution is to reduce the loop size, but the smaller loop will lead to inferior sensitivity. A measurement method to improve the spatial resolution of a magnetic probe was proposed in [14]. The basic principle of this measurement method is shown in Figure 2.3. A microstrip line is placed on xy-plane, and a loop is placed above the microstrip. The loop surface is parallel with yz-plane. Firstly, the probe scans along x-axis, and then the same probe shifts upward Δz distance and scans same DUT second time. The right-hand side of Figure 2.3 is equivalent difference of magnetic fields between two scanning measurement. If the shift distance Δz is much smaller then loop height, then $H\Delta S_2$ is much smaller then $H\Delta S_1$

and can be ignored. Then a virtual probe which has a smaller loop size ΔS_1 is accomplished by applying the subtraction. As we discussed before, spatial resolution is related to measurement height. This virtual probe has better resolution compare with original probe, as the loop structure is closer to DUT.

As actual loop size is not decreased, good sensitivity and spatial resolution can be achieved by using this measurement method. However, this measurement method requires double measurement time. Besides, a stable environment must be kept and radiation from DUT must be constant in the process of measurement. To solve these problems, a space difference magnetic near-field probe is proposed in [15]. The basic structure is shown in Figure 2.4.

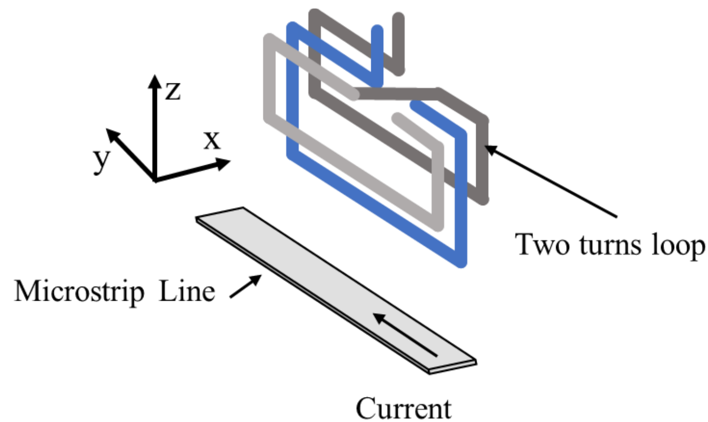

Figure 2.4 Structure of space different probe which can improve spatial resolution

This probe has two loop structures, one is one turn larger loop, the other is two turns loop. The loop size is optimized by simulation results, and probe has two output ports, which means the field information from these two loops is able to acquire by single measurement. According to simulation and measurement results, which are present in

[15], the distance between two dips is smaller after applying subtraction on two loops' data, which means space difference probe has higher spatial resolution.

Although the definition of spatial resolution is widely used, it still has limitation and disadvantages. Based on current definition, loop height which is related to measurement height is most important factor. Typical method of building high resolution probe is to reduce loop height and increase loop width to keep sufficient sensitivity. However, loop width also influences spatial resolution in measurement. In typical microstrip measurement, if coordinate system in Figure 2.3 is considered, H-field is constant along y-axis direction at certain height. In this situation, loop width doesn't affect spatial resolution.

In Section 3, the factors which affect spatial resolution and field distribution are discussed, and three dimensions of spatial resolution are put forward. Section 4 presents a better measurement setup to reflect spatial resolution. Then, an example is given to show how spatial resolution affect field distribution in near-field measurement.

3. SPATIAL RESOLUTION ANALYSIS

In real measurement, spatial resolution is not only related with probe, but also with DUT. If we only consider probe itself, then the spatial resolution reflects the similarity between original field and field measurement by probe. If the probe has high spatial resolution, then near-field pattern which is measured by probe should be similar to real pattern in space. As there are three dimensions in space, we put forward three dimensions of spatial resolution. These three dimensions are independent of each other.

3.1. FIRST DIMENSION OF SPATIAL RESOLUTION

Based on current definition, loop height which is related to measurement height is most important factor. The first dimension of spatial resolution is determined by loop height. In order to analysis spatial resolution and figure out how spatial resolution affects field distribution, microstrip and probe model are built in HFSS. Besides, an analytical model is designed for following discussions.

3.1.1. Microstrip Model. A HFSS 3D model of microstrip line is shown in Figure 3.1. The trace width is 16mil and thickness of dielectric is 8.9mil. Characteristic impedance is optimized to 50ohm. Two wave ports are added at both end of microstrip, and simulation results are shown in Figure 3.2. S11 and S21 results shows microstrip line is well designed.

To analysis near magnetic field distribution, a numerical model of microstrip is introduced [19]. For narrow microstrip line and high frequency signal, the skin effect has to be considered. An equivalent model is built with two current I1 and I2. I3 and I4 are images of I1 and I2 based on imaging theory, as shown in Figure 3.3.

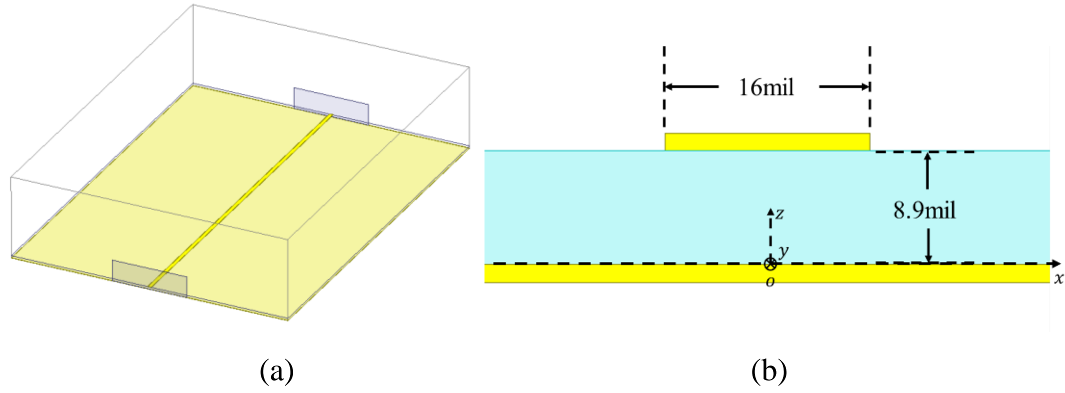

(a) (b)

Figure 3.1 (a) 3D model of microstrip line (b) cross-section view

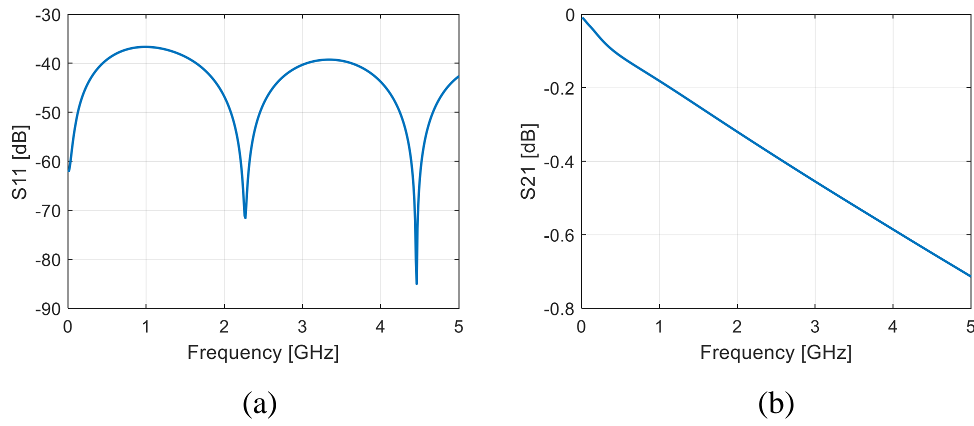

(a) (b)

Figure 3.2 (a) S11 (b) S21 of microstrip strip

The x-components of magnetic field is calculated by following equations:

$$H_x = H_{x1} + H_{x2} - H_{x3} - H_{x4} \quad (1)$$

$$H_{xi} = H_i \sin(\alpha_i) \quad (2)$$

$$H_i = \frac{I_i}{2\pi r_i} \quad (3)$$

$$r_i^2 = (x \pm W/2)^2 + h_i^2 \quad (4)$$

$$\sin(\alpha_i) = \frac{h_i}{r_i} \quad (5)$$

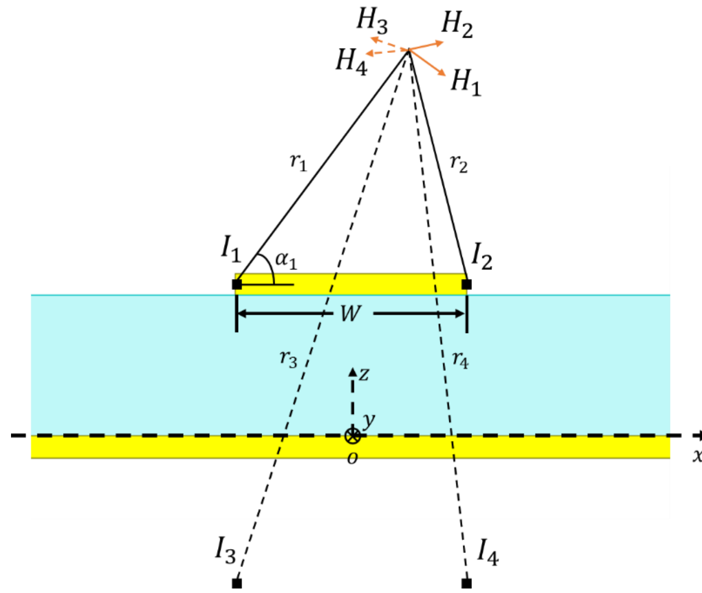

Figure 3.3 Numerical model of microstrip

The comparison of analytical and simulation results is shown in Figure 3.4. In HFSS, microstrip is from y=-20mm to y=20mm. The solution frequency is set to 1GHz, and Hx component is extracted at 1.61mm above microstrip at x, y=0mm location. There are little acceptable differences at the peak value and the locations of two dips, which means analytical result matches with simulation well.

The equations (3) is used to calculate magnetic field around an infinitely long straight wire, and microstrip line can be treated as long straight wires with current sources, as the length of microstrip is much larger than the distance between microstrip and measurement point. Therefore, in a small region along the y-axis direction, Hx field strength is almost constant when x and z are not change. In typical near-field probe test setup, probe is placed above the center of microstrip, and loop surface is parallel with y-z plane. If Hx strength map on loop surface is plotted, the field information should be one

dimensional: Hx strength changes along z-axis direction and keeps constant along y-axis direction. Then it can be assumed that loop width doesn't affect spatial resolution.

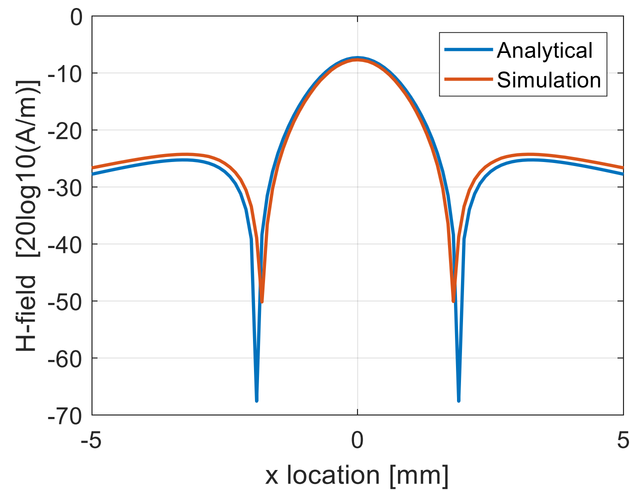

Figure 3.4 Comparison between analytical and simulation model

To verify the assumption, a numerical model of microstrip line with loop structure is introduced. The microstrip line model has been built in previous discussion, and a simple loop structure is added to the model, as shown in Figure 3.5.

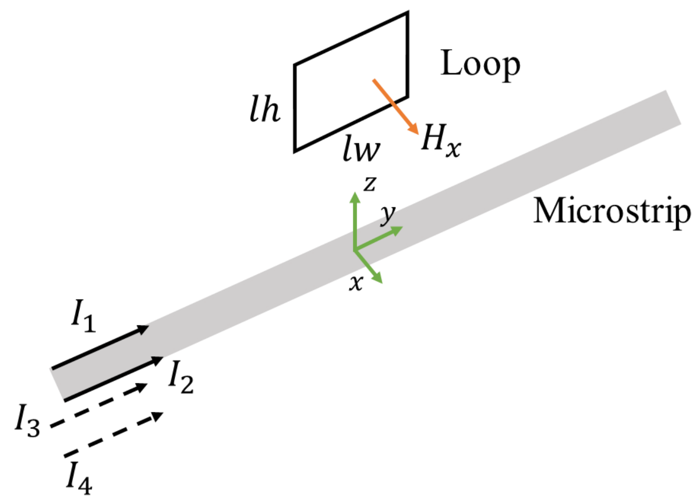

Figure 3.5 Schematic of analytical probe model

lw and lh are loop width and loop height values, separately. Voltage on loop can be calculated by following equations:

$$\oint_l E \cdot dl = -j\omega \iint_s B \cdot ds \tag{6}$$

$$V = -j\omega\mu \iint_s H_x \cdot ds \tag{7}$$

As H_x is coordinate dependent with x-axis and z-axis direction, independent with y-axis direction, equation can be written as:

$$V = -j\omega\mu \int_z^{z+lh} \int_{-lw/2}^{lw/2} H_x(x,z)dydz \tag{8}$$

Loop width is set to 0.5mm and 2mm, separately. Sweep x value, and voltage distribution are shown in Figure 3.6.

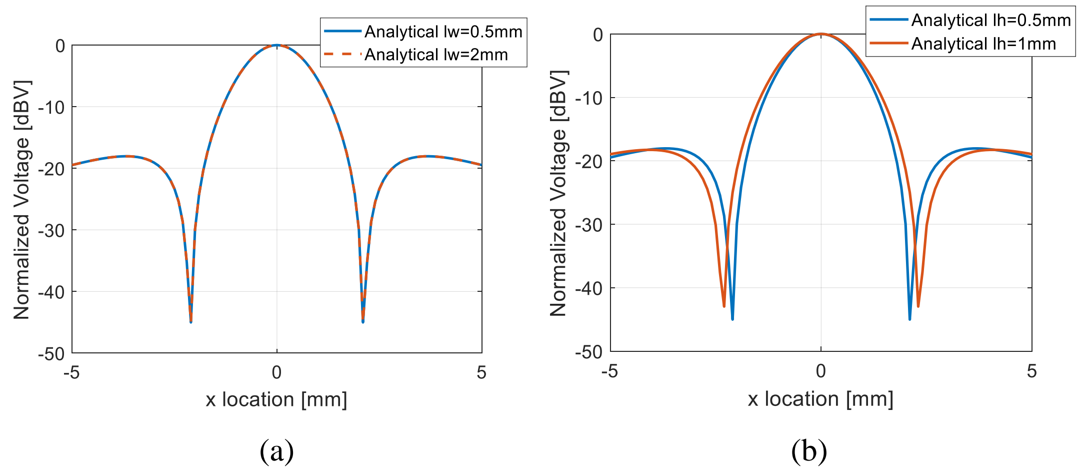

Figure 3.6 Comparison of voltage distribution between (a) different loop width and (b) different loop height

In Figure 3.6, voltage values are normalized. It shows that the distance of dips and -6dB points don't change, which means that ability of distinguish microstrip doesn't deteriorate. This result verifies our assumption and it shows that loop width factor doesn't

contribute to spatial resolution in typical measurement setup. The distance changes with loop height increasing, which is widely discussed in previous studies.

3.1.2. Probe Model. In order to analyze spatial resolution of actual probe, a simple probe model is built in HFSS, as shown in Figure 3.7. 4 layers PCB is designed, top layer and bottom layer are ground, and signal trace is on second layer. Two array vias is set on both side of probe tip, which are used to isolate E-field coupling. The symmetric ground structure also can suppress common-mode current, which are caused from the electric field in the z-axis direction. Initial Loop size is 0.5mmx0.5mm. Stack up and dielectric thickness is shown in Figure 3.7 (b). The width of Stripline is optimized to 5mil, with 50ohm characteristic impedance.

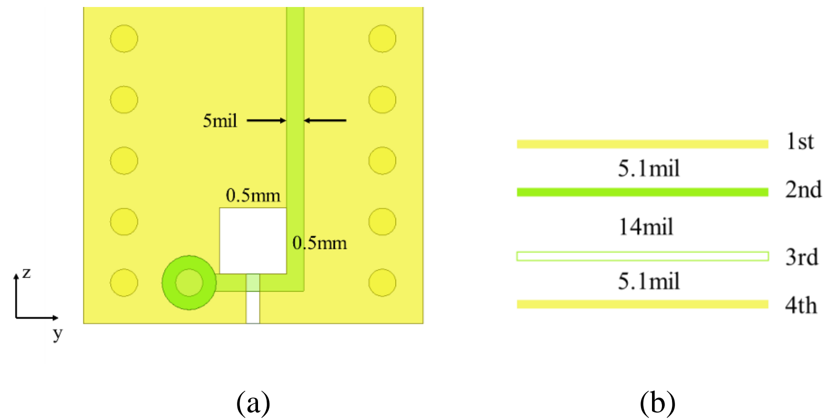

Figure 3.7 (a) Probe tip structure (b) stack-up information

Simulation model is shown in Figure 3.8 (a). In HFSS, wave ports are added on both end of microstrip and top of probe. The Frequency response is almost 20dB/dec increasing from low frequency to 1GHz, shown in Figure 3.8 (b), and still increases up to 5GHz, which means the probe can work up to 5GHz.

Simulation results are shown in Figure 3.9. Probe is placed above the microstrip and probe location is swept in x-axis direction from -5mm to 5mm. The solution frequency is set to 1GHz, which is within usable frequency of probe. The signal trace is on 2nd layer, which means probe is not symmetric, therefore the field distributions are not symmetric. Curves are shifted to keep the maximum value at x=0 location. It also shows that distance of dips doesn't change with loop width increasing, which is consistent with analytical results.

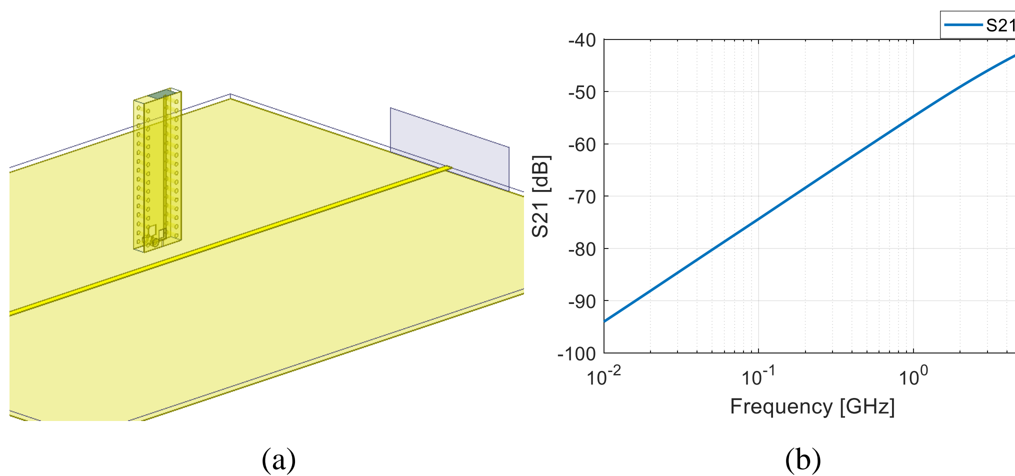

(a) (b)

Figure 3.8 (a) HFSS model (b) frequency response of probe

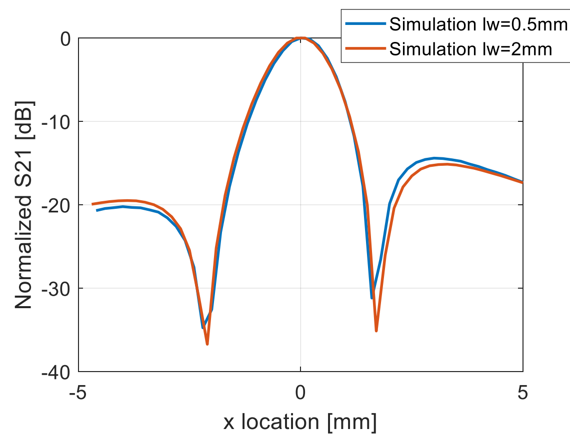

Figure 3.9 Comparison of simulation results between different loop width

3.2. SECOND DIMENSION OF SPATIAL RESOLUTION

In previous discussion, spatial resolution doesn't change with loop width increasing, in typical measurement setup. Hx field is constant along y-direction, and in Z-direction, as Hx field strength is related to height, the difference on loop height causes the difference of voltage distribution on loop, which affects spatial resolution.

To figure out the spatial resolution along y-axis direction, the loop is rotated 45 degrees around z-axis direction. In this situation, Hx component is coordinate dependent with y-axis, as field strength changes along the direction of loop width. This new numerical model is shown in Figure 3.10.

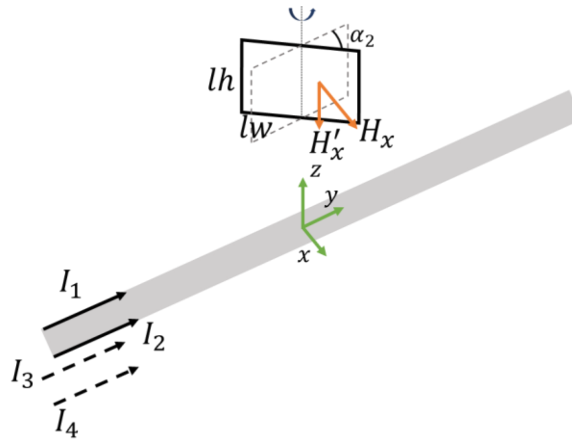

Figure 3.10 Numerical model after rotating 45 degrees

Voltage on Loop can be calculated by following equations:

$$H_x' = H_x \cos\alpha_2 \tag{9}$$

$$ds = dx/\sin\alpha_2 \, dz \tag{10}$$

$$V = -j\omega\mu \int_{z}^{z+lh} \int_{-lw/2\cdot\sin\alpha_2}^{lw/2\cdot\sin\alpha_2} H_x(x,z)\cos\alpha_2 \cdot dx/\sin\alpha_2 \, dz \tag{11}$$

The analytical results are shown in Figure 3.11. It shows that the distance of dips increases when a larger loop width is set. In simulation model, probe is also turned 45 degrees, and the result is shown in Figure 3.12 The simulation results are consistent with analytical results.

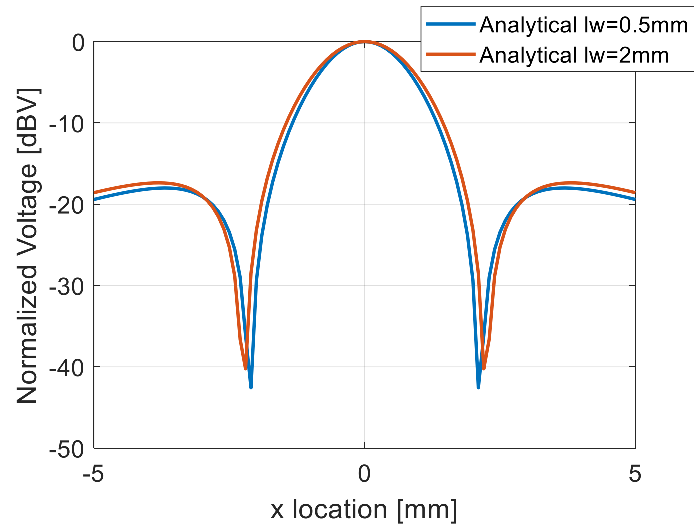

Figure 3.11 Comparison of analytical results between different loop width

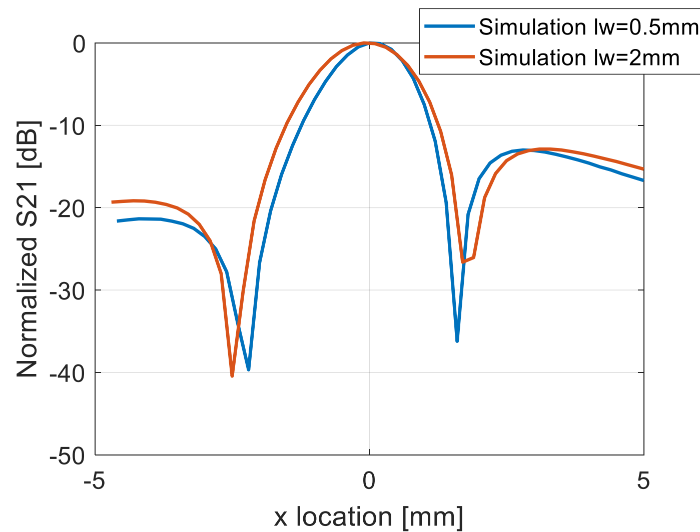

Figure 3.12 Comparison of simulation results between different loop width

After probe is rotated certain degrees, the field strength is different between left side and right side of loop, and then second dimension of spatial resolution which is determined by loop width is shown. Consider that there is a wide enough loop, which is even larger than the distance of two dips, then it is hard to see much different change of voltage when the probe is swept across the microstrip. This can be considered as an extreme condition of spatial resolution, and it is hard to distinguish microstrip in this situation. In actual measurement, probe may not be parallel with traces on DUT, and also, H-field strength along y-axis direction is not constant in most case. Loop width is able to impact the spatial resolution to further impact the resolution of field map.

3.3. THIRD DIMENSION OF SPATIAL RESOLUTION

Although the voltage is determined by H-field within whole loop region, it can be considered that the measured field is on same plane approximately, instead of three-dimensional area. The height of measurement plane is determined by electrical center of probe, and the electrical center may not be at same location as geometrical center [20]. A diagram of electrical center and geometrical center is shown in Figure 3.13.

The electrical center of the probe can be estimated by matching the simulated field distribution at different heights to the measured field distribution while the probe is scanning across the microstrip trace. The height which is the best match between simulation and measurement is an approximation of electrical height or measurement height. Although the probe which is shown in previous section is a simulation model, electrical center can be determined by matching the simulated field distribution at different heights to simulated voltage distribution on probe. Comparison results are shown in Figure 3.14.

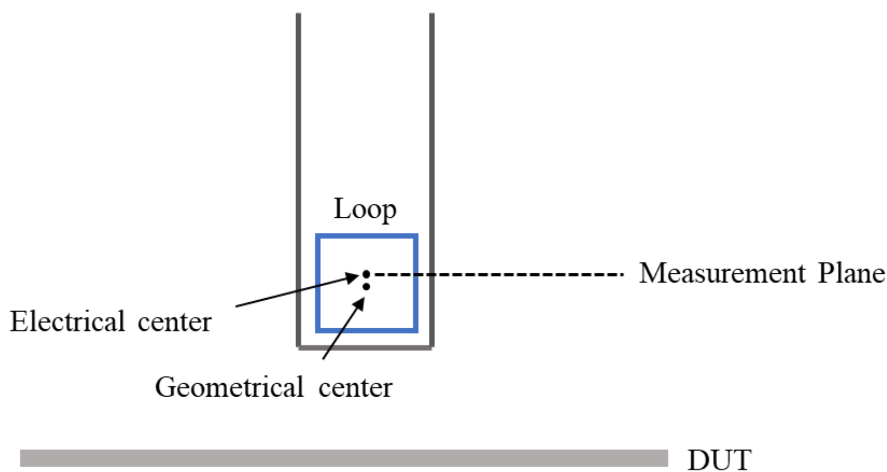

Figure 3.13 Diagram of electrical center and geometrical center

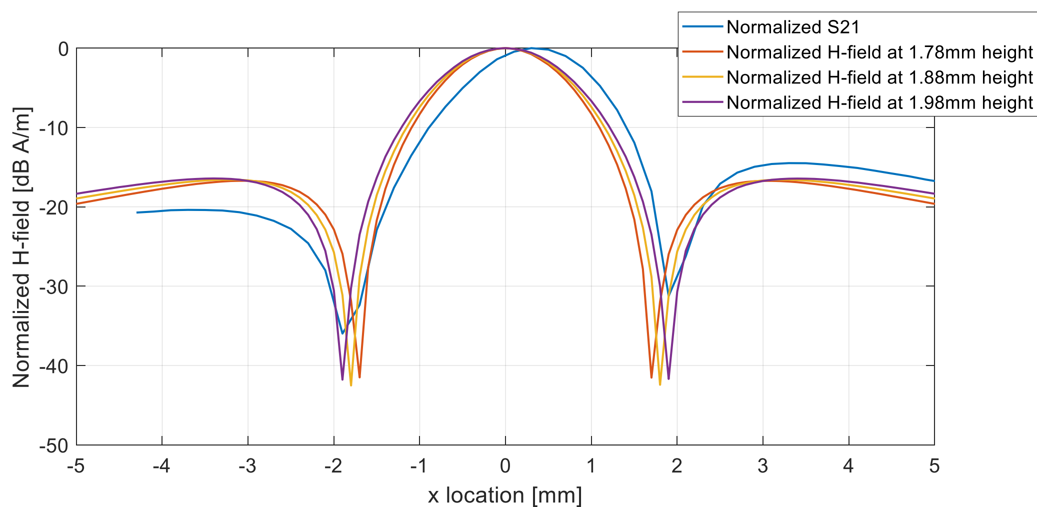

Figure 3.14 Tangential H-field strength across the trace at different heights (simulation and measurement)

In Figure 3.14, the 1.98mm height simulated field distribution match the simulated voltage distribution best, as the distances of two dips are same in both data. Consequently, we conclude that the electrical height is 1.98mm while the geometrical center's height is 1.88mm actually.

As the probe is asymmetric, the shape of voltage distribution is different with original field distribution. To compare with field distribution more clearly, we shift signal trace of probe to middle of the board, and keep the loop size and trace width same. Although characteristic impedance of transmission line is not 50ohm, the probe is still able to work up to 1GHz. Cross-section view and frequency response of probe are shown in Figure 3.15.

The probe is placed above microstrip at same height and voltage distribution which crossing the trace is simulated. As shown in Figure 3.16, the curve of voltage match very well with original field. This is an interesting result, which shows that voltage measured by probe reflects the original field perfectly. It means that this field shape is determined by DUT only, and spatial resolution doesn't affect shape of curve. The previous definition of spatial resolution is the distance between peak point and 6dB points, however, we are not sure that the distance is determined by character of probe, or only reflects the field distribution of DUT itself.

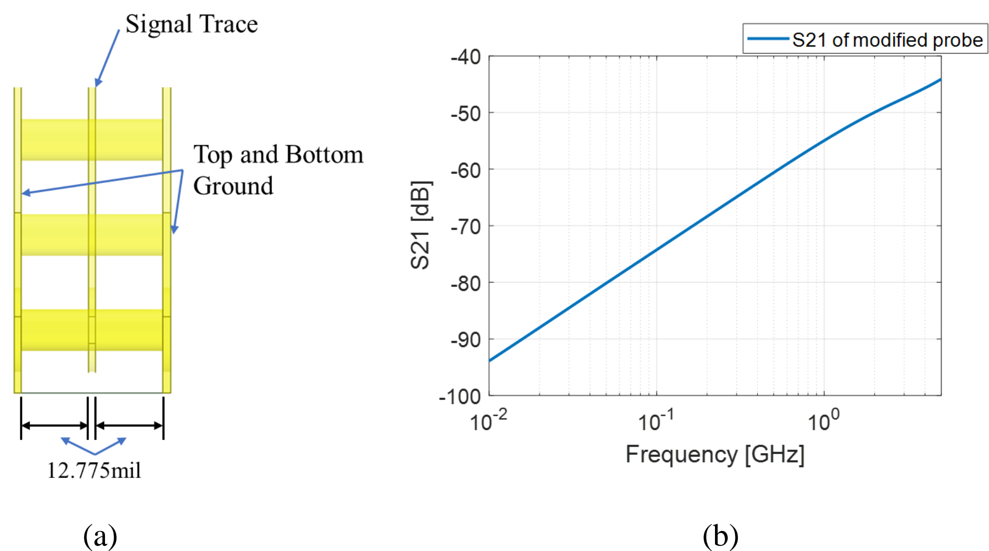

Figure 3.15 (a) Modified probe (b) frequency response

To explain this phenomenon, we modify the equation (7), which is used to calculate coupled voltage on loop. Voltage is proportional to $\iint_s H_x \cdot ds$, when frequency and permeability are not changed. In this integral equation, if ds is not considered as infinity small and is replaced by Δs, assuming H_x is constant in the area of Δs, then the equation can be written as:

$$V \approx -j\omega\mu \sum_{j=1}^{m} \sum_{i=1}^{n} H_{x(i,j)} \cdot \Delta s_{(i,j)} \quad (12)$$

The schematic of this calculation is shown in Figure 3.17. An approximate voltage is calculated by adding all $H_x \cdot \Delta s$ in loop area. In previous section, two dimensions of spatial resolution are already introduced, which are related to loop height and loop width, respectively. If Hx field strength changes in both y and z-axis directions, as shown in Figure 3.17, and area of Δs is fixed, then spatial resolution is related to amount of Δs in both directions. This relationship between spatial resolution and loop size can be demonstrated by smoothing a one-dimensional array. Assume that there is one-dimensional random array, as shown in Table 3.1.

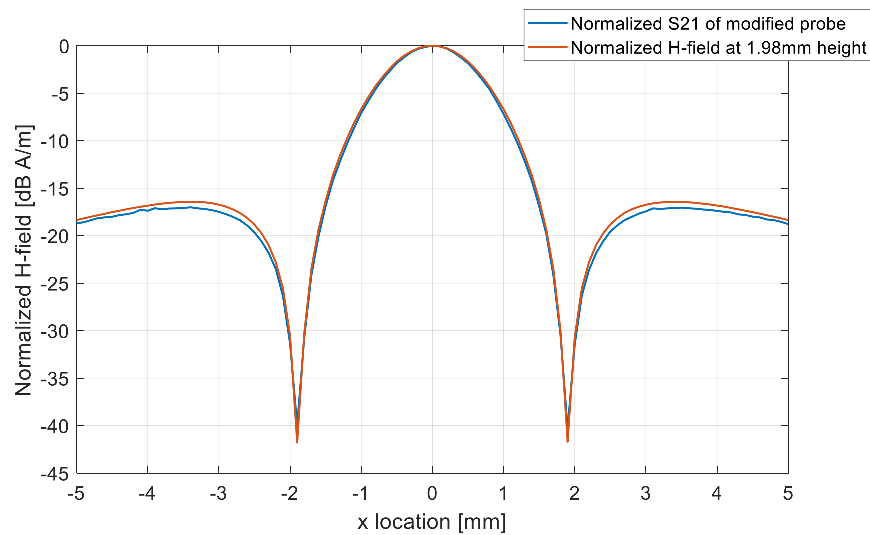

Figure 3.16 Tangential H-field strength measured by probe and original field

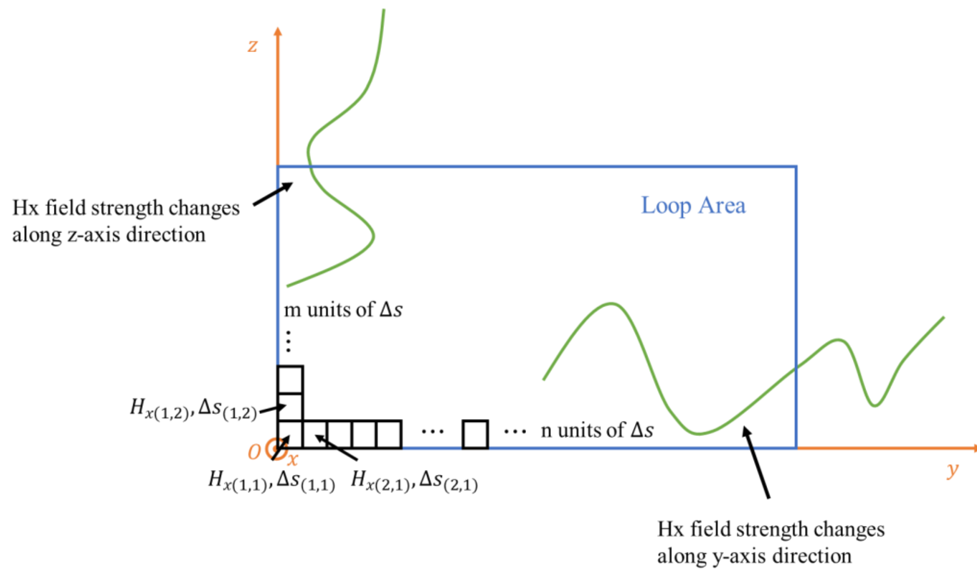

Figure 3.17 Schematic of approximate voltage calculation

Table 3.1 Original one-dimensional array

Sequences	Values	Sequences	Values
1	65.04	6	52.51
2	64.80	7	41.58
3	51.78	8	46.11
4	59.15	9	52.00
5	56.37	…	…

Then, a new array is constructed by averaging 5 numbers' value. The value of 1st number is equal to average value of 1st to 5th values in original array, and the value of 2nd number is the average value of 2nd to 6th values, and so on. New array is shown in Table 3.2.

Figures of initial array and modified array are shown in Figure 3.18. It shows that after averaging operation, the trend curve of this one-dimensional array become

'smoothness'. However, some peaks or dips are lost, and the shape of curve is not sharp anymore.

Table 3.2 New one-dimensional array after smoothing

Sequences	Values	Sequences	Values
1	59.43	6	47.93
2	56.92	7	46.50
3	52.28	8	47.31
4	51.14	9	46.83
5	49.71	…	…

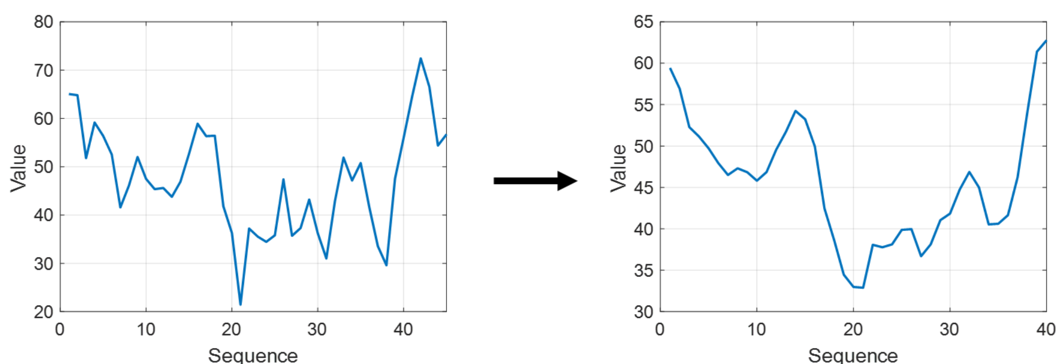

Figure 3.18 Smoothing on one-dimensional array

The influence of loop size on spatial resolution is similar to averaging operation. If loop width or height is small enough, spatial resolution along width or height direction will be good enough and the field distribution measured by probe will reflect the actual field perfectly. With loop size increasing, more magnetic field is coupled into the loop. The magnetic field within the whole loop area is integrated as one voltage, therefore probe is not able to distinguish ripples of magnetic field strength in a small area.

The spatial resolution along y-axis and z-axis directions are determined by loop width and loop height, respectively. In Figure 3.16, Hx-field distribution is along x-axis direction, which is perpendicular to loop surface. As the probe is only one turn, and copper thickness is very thin and can be ignored, there is not ‘averaging operation’ along x-axis direction, which means spatial resolution along x-axis direction is extremely good. When probe is moving across microstrip trace, the voltage measured by probe is able to match with original field perfectly, as long as step length of scanning is small enough.

Here we put forward third dimension of spatial resolution, which is determined by thickness of multiple turns of loop. In analytical model, another loop is added as the second turn of original loop. Total voltage is the sum of voltage on each loop:

$$V = V_1 + V_2 \tag{13}$$

Loop width and Loop height keep same value, and the analytical model is shown in Figure 3.19.

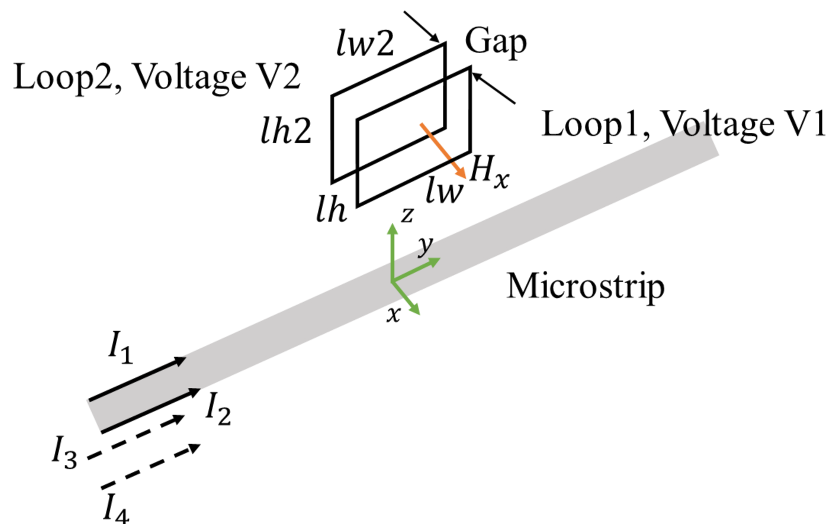

Figure 3.19 Analytical model of two turns loop

Comparisons between one turn loop and two turns loop are shown in Figure 3.20. When the probe has multiple turns, 6dB points locations change and the distance between two dips increases. With the gap between two turns increasing, the distance between two dips also increases. It shows that spatial resolution is affected by multiple turns and the total thickness of all turns.

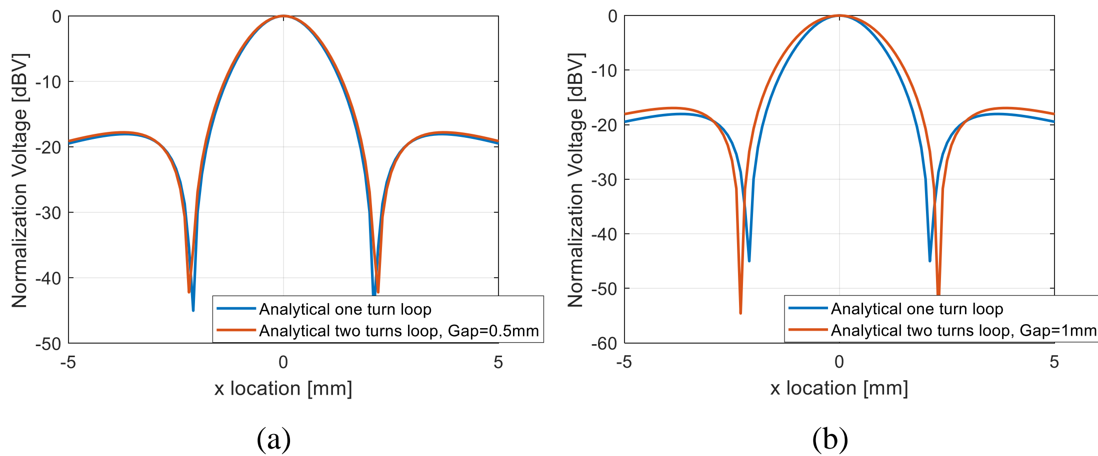

Figure 3.20 Comparison of analytical results between one turn and two turn loops: (a) Gap=0.5mm (b) Gap=1mm

In simulation model, two turns loop is designed. A signal via is added to connect second layer trace and third layer trace. The loop size is still 0.5mmx0.5mm, and the simulation model of two turns probe is shown in Figure 3.21.

Probe location is swept in x-axis direction from -5mm to 5mm. Probe is 0.5mm above DUT, instead of 1mm, to make the difference between field distributions more clearly. For convenience of comparison, the modified symmetry probe is used as reference. The comparison of field distribution between one turn symmetry probe and two turns probe are shown in Figure 3.22.

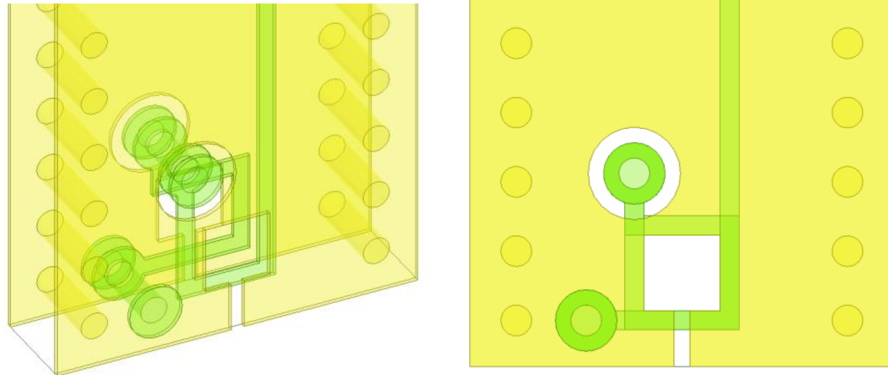

Figure 3.21 Structure of two turn loops in simulation model

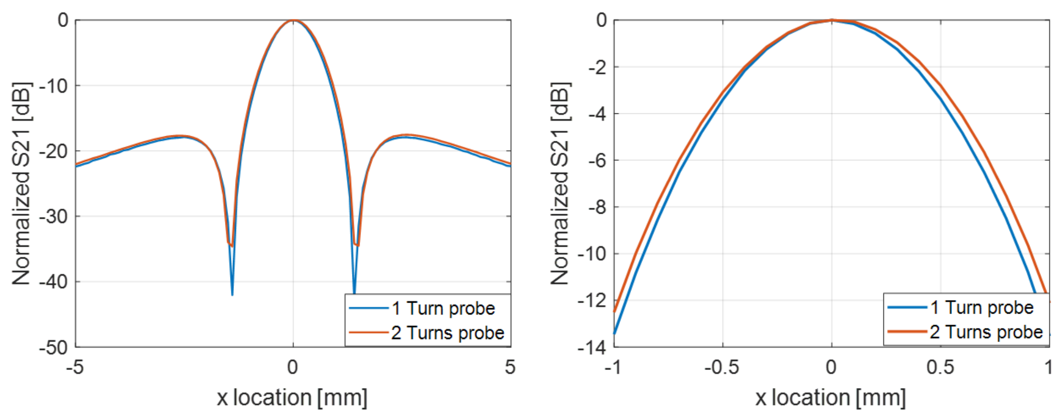

Figure 3.22 Voltage distribution simulated by 1 turn and 2 turns probe

As the distance between two loops is only 14mil (dielectric thickness between 2nd layer and 3rd layer), there is a little difference between fields distribution of one turn and two turns loop.

To make the difference clearer, we increase dielectric thickness between 2nd layer and 3rd layer, from 14mil to 30mil, and keep same values of loop size and trace width. The dielectric thickness of reference symmetry probe is also changed. Cross view of these probes is shown in Figure 3.23.

Comparison between 1 turn and 2 turns thicker probes are shown in Figure 3.24 (a). As the probe is thicker and the distance between two turns increases, the difference of field distributions between single turn and 2 turns probe cannot be ignored. It proves that spatial resolution is related to thickness of all turns. In Figure 3.24 (b), it shows that even the probe is much thicker, spatial resolution is almost not influenced as long as the loop is only one turn. In actual probe design, if multiple turns structure is designed and total thickness of turns is larger than 30mil, based on simulation results, third dimension of spatial resolution which is related to loop turns need to be considered.

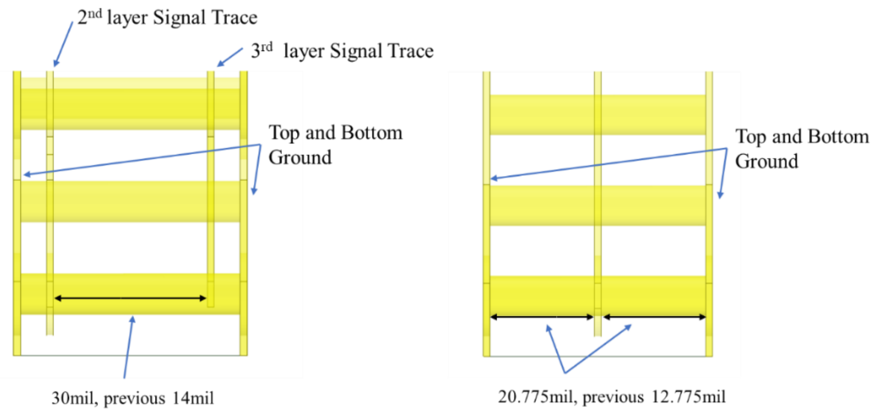

Figure 3.23 Structure of modified wider probe

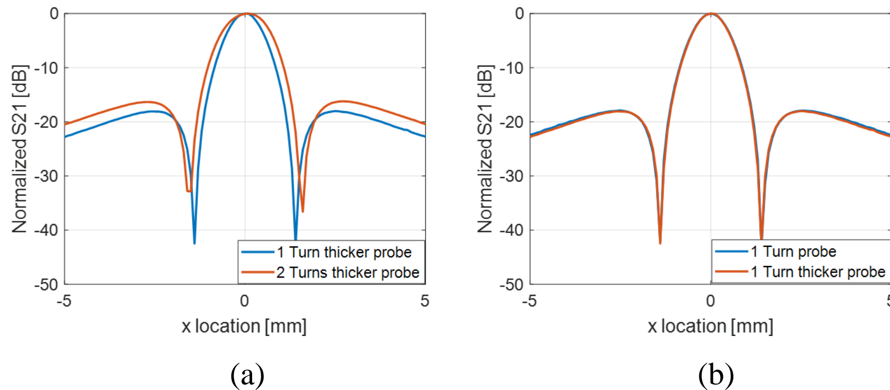

Figure 3.24 (a) Simulated voltage distribution of 1 turn and 2 turns probe (b) results comparison between 1 turn and 1 turn thicker probe

4. OPTIMIZED MEASUREMENT SETUP OF SPATIAL RESOLUTION

In previous sections, we discuss three dimensions of spatial resolution, which are determined by loop height along z-axis direction, loop width along y-axis direction, and total thickness of multiple turns along x-axis direction, respectively. Typical definition of spatial resolution is the distance between peak point and 6dB points, and in measurement setup, the probe is placed above microstrip trace, and loop surface is parallel with trace direction. However, one dimensional of spatial resolution which is determined by loop width is not able to be shown in this measurement, as Hx field is constant along loop width direction. In this section, a bend microstrip is designed as the DUT to replaced microstrip, as bend microstrip is able to generate varied Hx field along x, y and z-axis directions at the corner area.

Simulation model is shown in Figure 4.1. Trace width is set to 14mil and characteristic impedance is optimized to 50ohm. Wave ports are added on both end of microstrip. Two perpendicular sheets are added above microstrip at corner area, which are used to add mesh to make H field accurate within interested area.

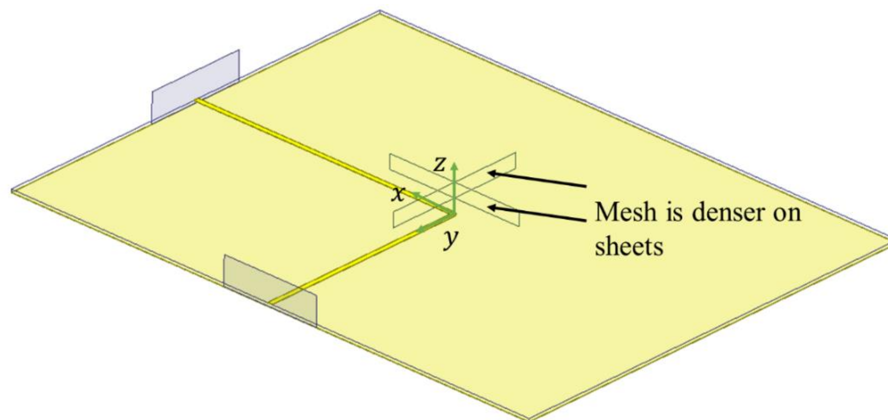

Figure 4.1 Bend microstrip model

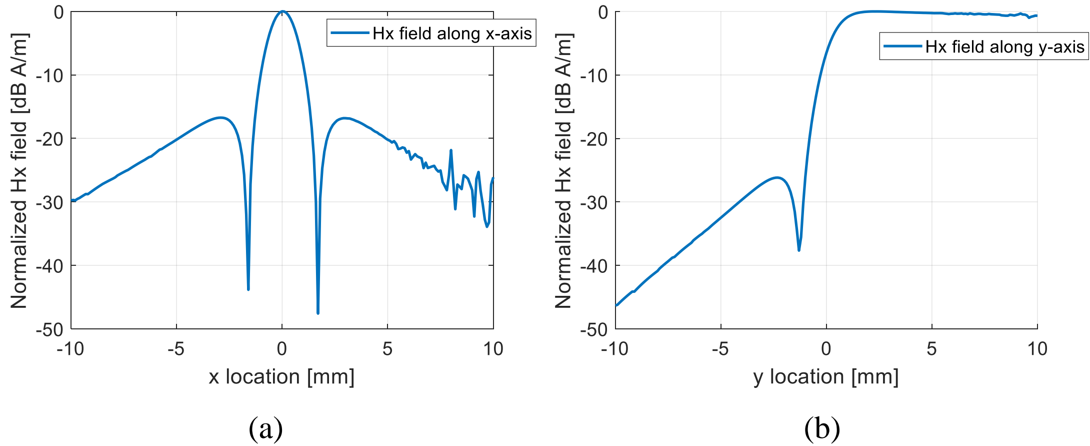

(a) (b)

Figure 4.2 Hx field distribution along x-axis (a) and y-axis (b)

Hx field along x-axis and y-axis direction are shown in Figure 4.2 (a) and (b), respectively. Hx field is calculated at 1.7mm above bend microstrip. In Figure 4.2 (a), there is some ripples of Hx field strength when x is larger than 5mm, due to the bend microstrip structure and non-TEM mode at the corner. In Figure 4.2 (b), as center of microstrip trace is placed at y=0mm, Hx field strength decrease quickly along y-axis negative.

As the mesh is dense enough, the field information within sheets can be used in analytical model. We calculate Hx field in y-z plane in HFSS and generate a matrix, which includes locations, and real part and image part of Hx field at each location. The step length in both y-axis and z-axis is set to 0.01mm. Similar to equation (), an approximate voltage on loop is calculated by adding all $H_x \cdot \Delta s$ in loop area. The loop scans from y=-5mm to y=-5mm at certain height. Loop surface is parallel with y-z plane. Comparisons of Hx field distribution along y-axis direction between different loop sizes are shown in Figure 4.3.

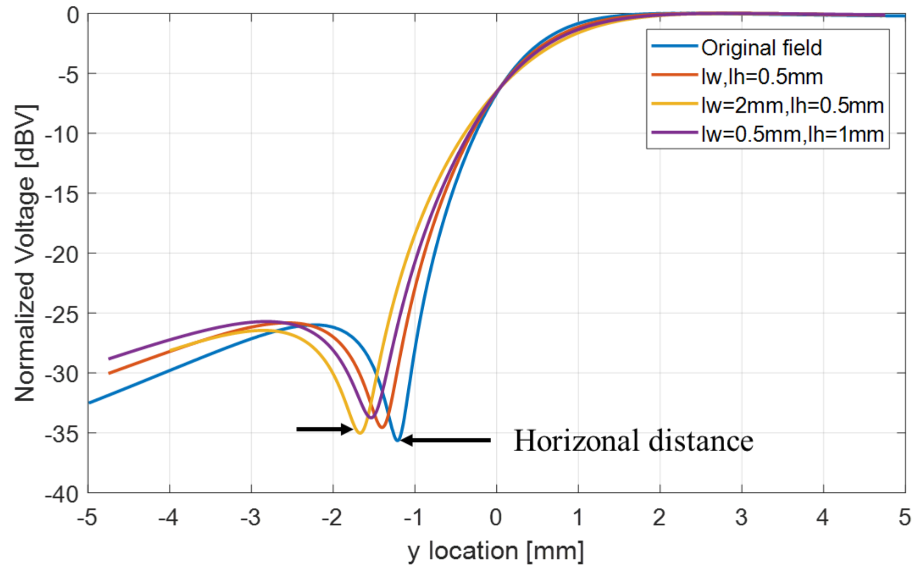

Figure 4.3 Hx-field distribution along y-axis

In analytical model, the bottom of loop is fixed at certain height, and the simulated height of original field is same as the height from 0.5x0.5mm loop center to DUT. In Figure 4.3, it shows that the location of dip moves along negative y-axis direction with loop size increasing, which means spatial resolution become worse. The horizonal distance between the dip of original field and the dip of field measured by loop can be treated as relative spatial resolution. When loop is infinite small, the distance approaches zero and spatial resolution is perfect. Effect of spatial resolution along y-axis and z-axis which are determined by loop width and loop height respectively can be shown in this setup. As the field measured by probe can be considered as the field at electrical height, the spatial resolution in z-axis direction doesn't contribute to field distribution. However, electrical height is related to loop height, when the height from bottom of probe to DUT is fixed. So spatial resolution can be increased by reducing loop height. This improvement of spatial resolution is related to characteristic of DUT, instead of probe itself.

In HFSS, a bend microstrip with probe is built. The probe is placed above microstrip at certain height, and it moves from y=-5mm to y=5mm, shown in Figure 4.4.

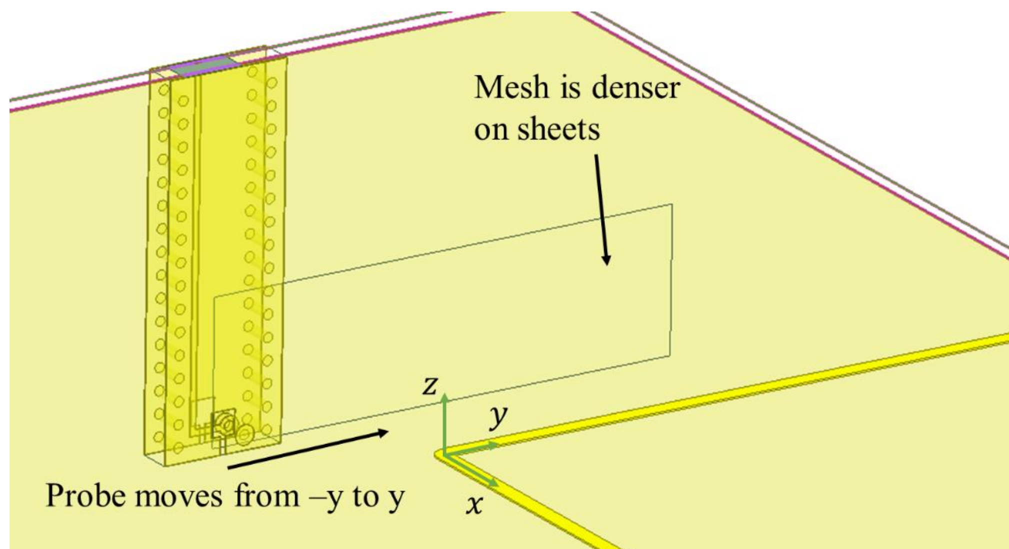

Figure 4.4 Simulation model of bend microstrip and probe

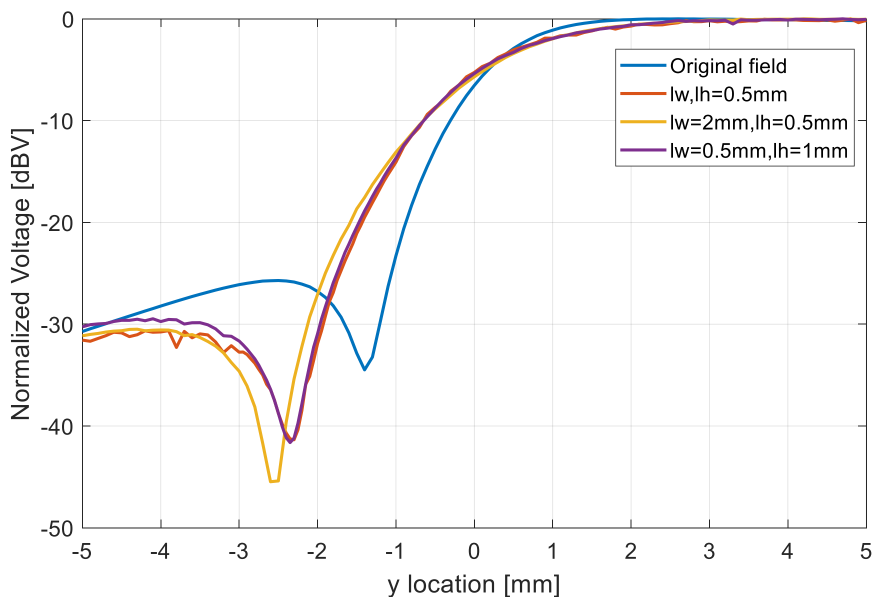

Figure 4.5 Hx-field distribution along y-axis (original field and the field measured by probes)

Comparison between original field distribution and voltage distribution of probe is shown in Figure 4.5. It shows that the location of dip moves along negative y-axis direction with loop size increasing. As E-field is also coupled to probe at the corner area, the locations of dips are different compare with analytical model.

To see the spatial resolution effect of multiple turns, we need to scan along x-axis direction at the corner or across the straight trace. This is similar to the setup which is shown in Figure 3.19. Therefore, three dimensions of spatial resolution can be shown by measuring twice under bend microstrip.

5. EFFECT OF SPATIAL RESOLUTION IN NEAR-FIELD MEASUREMENT

To figure out the actual effect of spatial resolution in near-field measurement, an actual DUT is built in HFSS. The DUT is cut and imported from board file, as shown in Figure 5.1. The board has 8 layers. Layer 2, 4, 5 and 6 are ground layer, and Layer 3 and 6 is used for signal line. In this part of board, 4 striplines are at layer 3, and connect to pads on bottom layer through signal vias. There are four 50-ohm resistors are soldered between signal pads and ground pads on bottom layer. Therefore, 4 striplines are terminated by 50-ohm resistors to reduce crosstalk coupled to others traces.

In HFSS, 4 lumped elements are used on replace 50ohm, and 4 wave ports are added at the edge of each traces. 4 traces are all excited by 1 incident voltage with same phase, to simulate the real condition.

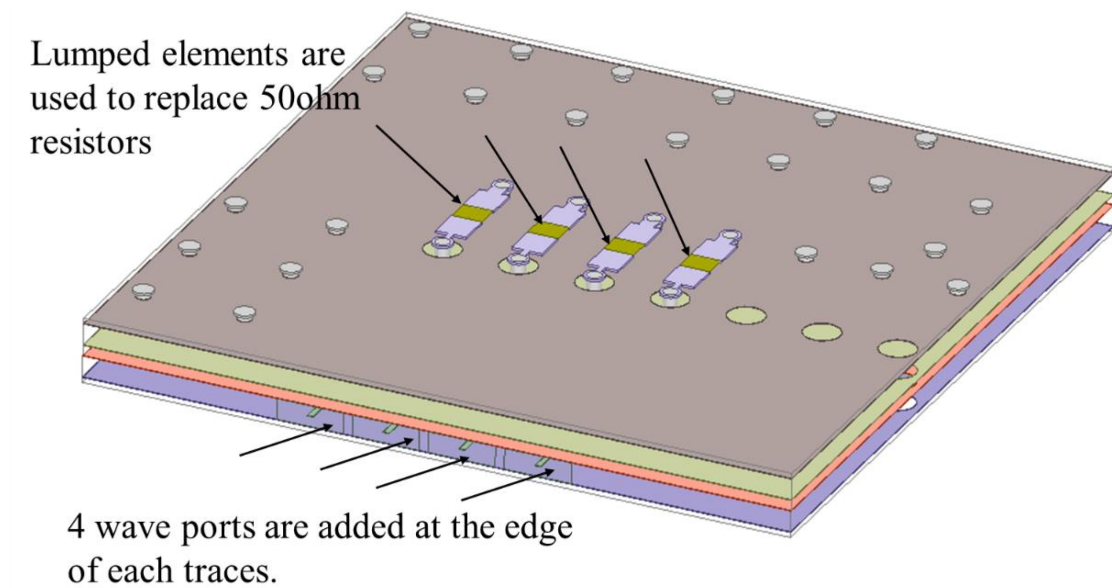

Figure 5.1 Part of a board model with 4 resistors

The probe is placed above this DUT. The distance between the bottom of probe and DUT is 1mm. As spatial resolution in z-axis direction doesn't contribute to field distribution, two probes which have different loop width are used for near-field scan. The scan area and probe model are shown in Figure 5.2. The scan area is from (0, -4) to (3, 4), and parallels with x-y plane. Hy-field component is measured in this setup.

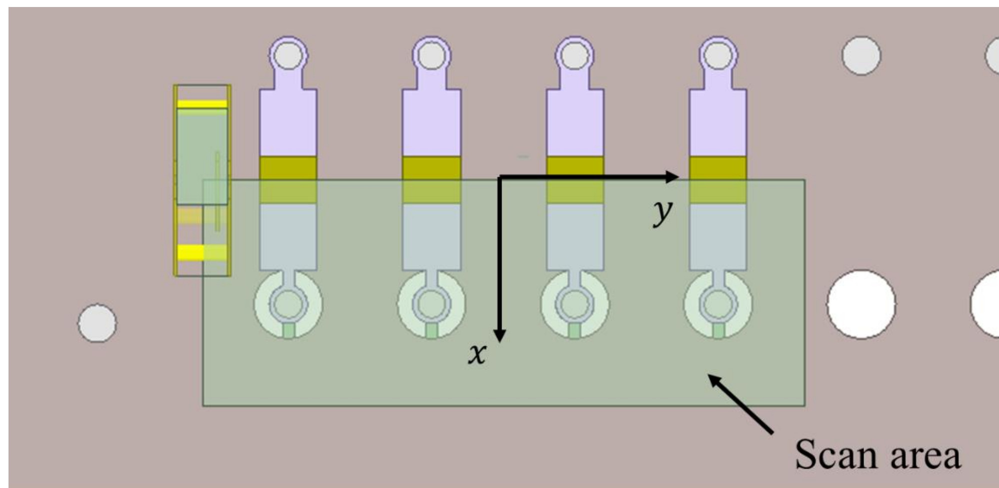

Figure 5.2 Scan area in simulated near-field measurement

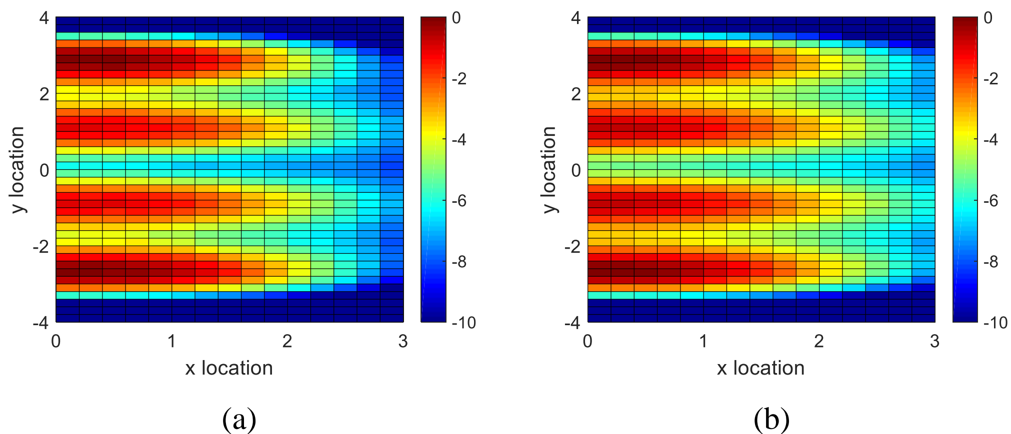

Figure 5.3 Simulated field distribution by different probes: (a) 0.5mm loop width (b) 2mm loop width

Simulated results are shown in Figure 5.3. Figure 5.3 (a) is field distribution measured by 0.5mm loop width probe, and Figure 5.3 (b) is the field distribution measured by 2mm loop width probe. Voltages are normalized to 0dBm, and the scale are same in both plots. It is easier to distinguish 4 traces using the field distribution measured by 0.5mm probe, compare with 2mm probe. The field strength at the gap of two traces is lower and along positive x-axis direction, the field strength decreases when x value is smaller. The field distribution measured by 0.5mm probe closes to original field distribution of DUT, and it shows that in actual near-field measurement, spatial resolution does affect field distribution. These three dimensions of spatial resolution need to be considered in probe design.

6. SUMMARY

In this section, typical definition of spatial resolution is introduced first. Although the definition is straight forward and easy to understand, it cannot reflect spatial resolution of probe properly. Therefore, the impacts of spatial resolution are studied by using analytical and HFSS model of microstrip strip and probe. Three dimensions of spatial resolution is presented and discussed. When loop surface is parallel with y-z plane and the probe is used to measure Hx field, the spatial resolution is determined by loop height, loop width and thickness of multiple turns in z-axis, y-axis and x-axis directions respectively, as shown in Figure 6.1. As the field measured by probe can be considered as the field at electrical height, the spatial resolution in z-axis direction of probe doesn't contribute to field distribution. However, spatial resolution can be increased by reducing loop height, and this improvement of spatial resolution is related to characteristic of DUT, instead of probe itself.

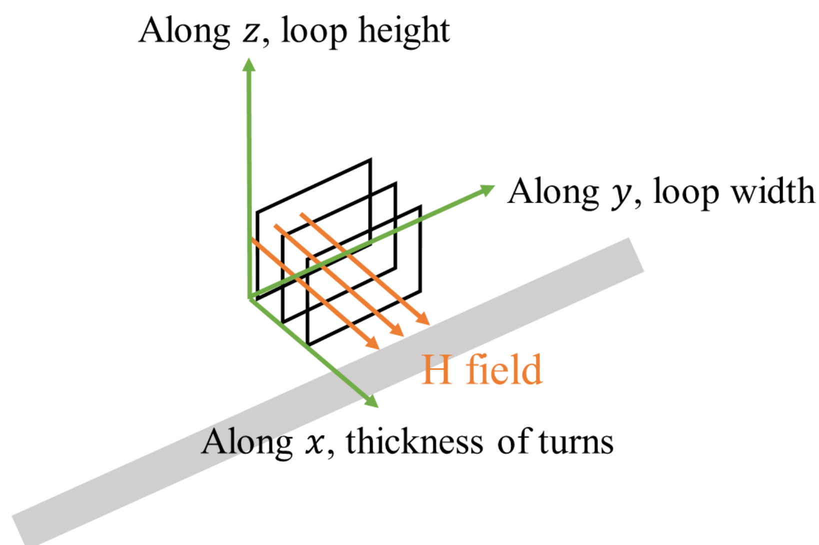

Figure 6.1 Three dimensions of spatial resolution

Moreover, a bend microstrip model is designed and used as DUT in spatial resolution measurement. As bend microstrip is able to generate varied Hx field along x, y and z-axis directions, three dimensions of spatial resolution can be shown by measuring along x-axis and y-axis directions under bend microstrip.

In the end, an actual board is used to show the effect of spatial resolution in near-field measurement. Two probes which have different loop width are used, and scan a certain area above DUT. The simulation results show than it is easier to distinguish 4 traces using the field distribution measured by 0.5mm loop width probe, compare with 2mm probe. In actual near-field measurement, spatial resolution affects field distribution, so in probe design, these three dimensions of spatial resolution need to be carefully considered based on different requirement.

PAPER

I. A 20GHZ LANDING PROBE DESIGN BASED ON POGO-PINS

Xin Yan[#1], Yansheng Wang[#2], Jianchi Zhou[#3], Tun Li[*4], and Jun Fan[#5]
[#]EMC Laboratory, Missouri University of Science and Technology
4000 Enterprise Dr, Rolla, MO, USA
[5]jfan@mst.edu
[*]ConvenientPower Systems, Chengdu, China

ABSTRACT

A landing probe design is proposed in this paper based on pogo-pins. Landing probes are usually used to obtain TDR and S-parameters of the device under test (DUT) so that the performance of the DUT can be evaluated. This design has two major advantages. First, it is durable. Second, it can be easily integrated into automated testing systems. The designed probe works well up to 20 GHz, which is validated by measurement.

Keywords—Landing probes; Pogo-pin; Landing Pad; Signal Integrity (SI)

1. INTRODUCTION

With the rapid advancement in electronic technologies, the trend of printed circuit board (PCB) and flex designs is moving toward higher and higher frequency and more and more compact form factor. This trend, though brings in various benefits for users, makes the PCB and flex designs more and more vulnerable to signal integrity (SI) [1]-[3] and electromagnetic compatibility (EMC) issues [4], [5].

To evaluate the PCB and flex design and debug SI and EMC related issues, measurements are conducted using probes including field probes such as electric field probes [6], [7], magnetic field probes [8] and landing probes [9]. Field probes are usually used for near-field pattern acquisition over PCB or flex, which in turn provides insights of trace routing, layout, component radiation properties etc. Field probes are widely studied and are not the focus of this paper. The landing probe is generally employed for S-parameter and TDR measurement [10], [11]. The device under test (DUT) for the landing probe is usually narrow traces.

Conventionally, a landing probe is made of a coaxial cable with the inner conductor extended out and a pad attached to the out conductor at the tip of the coaxial cable. There are several drawbacks of this design. First, the tip is fragile and can be easily damaged. Second, it is difficult to land the probe tip evenly onto the DUT. Sometimes, this is due to the rotation of the probe tip; while at other times, it is caused by the deformation of the DUT surface. All these short-comings confine the usage of the conventional landing probe to only well-trained experimenters and refrain it from testing automation.

To resolve the disadvantages in the traditional landing probes, a new probe design utilizing the pogo-pin is proposed in this paper. In the new design, the probe tip is durable. Besides, the compression tolerance of a pogo-pin enables the new probe to be integrated into probing stations for automatic landing tests. This probe is demonstrated working well up to 20 GHz.

The rest of the paper is organized as follows. In Section 2, the design method of the landing probe is introduced. In Section 3 measurement variation for the designed probe is presented. Section 4 concludes the paper.

2. DESIGN OF THE LANDING PROBE

2.1. POGO-PIN

Pogo pins showed excellent electric and mechanical performance when serving as the high-speed interconnects transferring electric signals from the probe to the DUT [12]. In this work, pogo-pins are used to replace the metal tips of a traditional landing probe.

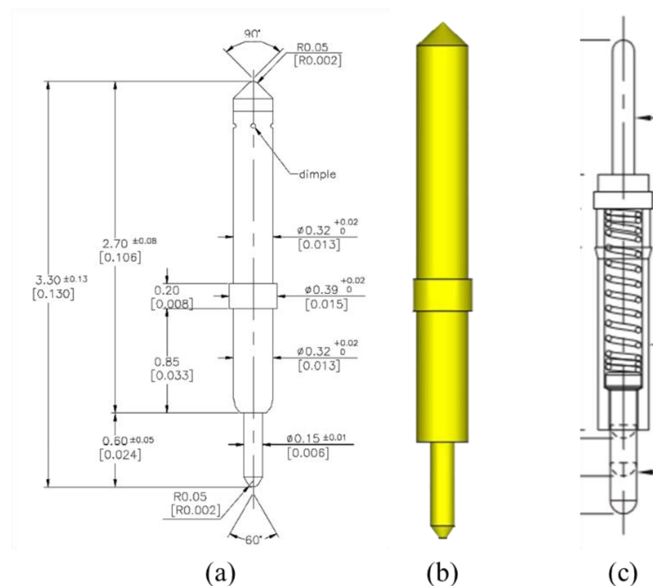

Figure 1 (a) Specification of a pogo-pin [13] (b) simplified 3D model of a pogo-pin (c) cross-sectional view of a pogo-pin [14]

The specification of a pogo-pin used in this probe design is shown in Figure 1 (a). The body of the pogo-pin is gold plated. The insertion loss of the pogo-pin is about -1dB at 9.69GHz [13]. Figure 1 (b) shows the simplified 3D model in CST, which consists of solid structure. The geometrical dimensions follow the specification in Figure 1 (a). The spring structure inside the body of the pogo-pin is completely hidden by the above-mentioned solid structure. The spring structure can be seen in Figure 1 (c). Due to the

skin effect, it is reasonable to assume the current flowing only on the outer surface of the pogo-pin at high frequency.

2.2. PROBE

The dimensions of the probe are shown in Figure 2 (a). The probe is based on coplanar waveguide with ground (CPWG) structure. The top layer is the signal layer. The second, third, and bottom layers are ground layers. A CPWG structure requires only two layers, the first signal layer and the second ground layer. However, a two-layer design is so thin that the probe may easily break. A four-layer design is employed instead only to enhance its mechanical strength. The third and fourth layers are not necessary to maintain the performance of the CWPG. Dielectric material is FR4.

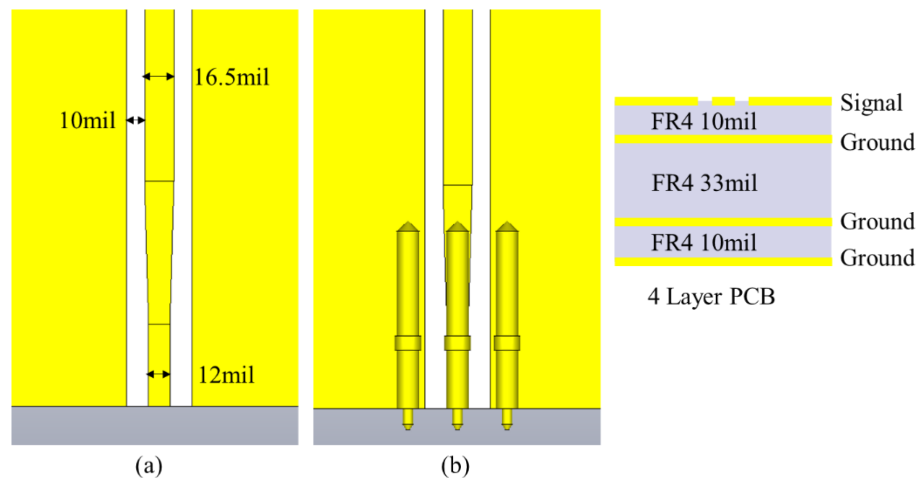

Figure 2 (a) Dimensions of the probe with pogo-pins (b) and stack-up information

In this probe design, pogo-pins are fixed at the end of board (shown in Figure 2 (b)) as the probe tip. One pogo-pin is fixed on the trace, and two pogo-pins are on both side ground planes. This ground-signal-ground (G-S-G) structure is used to relieve the

discontinuity effect of the transition from the probe to the DUT. The characteristic impedance of a transmission line is calculated as [15]:

$$Z_0 = \sqrt{\frac{R+j\omega L}{G+jwC}} \tag{1}$$

As the frequency increases, the values of $j\omega L$ and $j\omega$C increase, while R and G are negligible within the frequencies of interest. The characteristic impedance is related to the radio of per-unit-length (p.u.l) inductance and p.u.l capacitance, approximately. The characteristic impedance of the CPWG trace is designed to be 50ohm. For the probe tip, 50 Ohm should be maintained for the pogo-pin structure. However, when the pogo-pin structure is soldered onto the CPWG, the p.u.l capacitance increases for that region and thus the characteristic impedance decreases below 50 Ohm. For the pogo-pin tips which extend out of the end of the CPWG, usually the characteristic impedance is higher than 50 Ohm. Clearly, there is a fluctuation of the characteristic impedance around the probe tip.

To reduce the effect of discontinuity, a tapering structure is introduced at the tip region. The trace width is gradually reduced from 16.5 mil to 12mil to decrease the p.u.l capacitance. The separation of pogo-pins has also been optimized. To simulate the real condition where the probe lands on the DUT, the length of the pogo-pin tip decreases to half of its original length, which mimics the compression of the spring after landing.

2.3. LANDING PROBE

The structure of the landing board is similar to the probe. The trace width and gap are the same as the probe. The probe is supposed to land at one end of the landing board. The other end of the landing board is connected to a SMA connector.

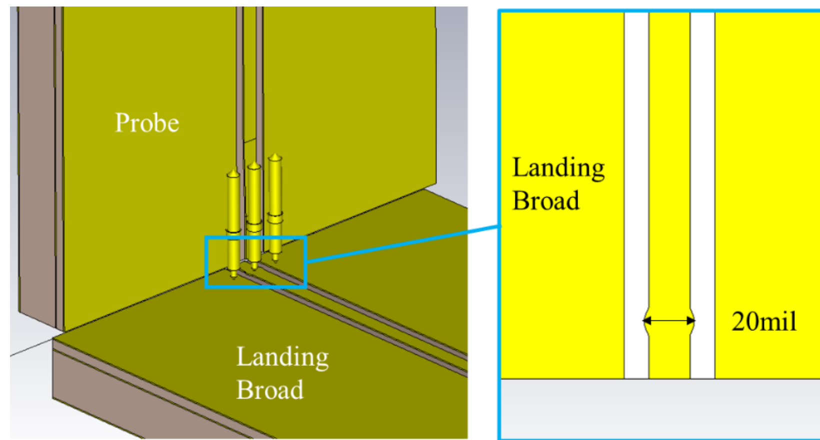

Figure 3 A landing pad is added at the landing position

The transition from the probe to the DUT is optimized, since the characteristic impedance mismatches at the transition. In more cases, landing pads are required. The design of the landing pads has a significant impact on the overall performance of the measurement system. The previous study showed that the optimized landing pad enabled good transition performance up to 90GHz [16]. Since the characteristic impedance of the pogo-pin tip is higher than 50ohm, the landing pads are used to reduce the characteristic impedance at the landing position. In this paper, a circular pad is added to trace of landing board at landing position, which is shown in Figure 3. The diameter of landing pad is larger than the width of trace, which reduces the effect of impedance discontinuity introduced by the pogo-pin tip. Diameter of pad is optimized to 20mil by full-wave simulations.

3. MEASUREMENT VALIDATION

A probe and a landing board are fabricated as shown in Figure 4 (a) and (b), respectively. Pogo-pins are soldered at one side of the probe, and the tips are stretched out of the board. The landing board is built with different diameters of landing pad, which are 20mil, 22mil, and 24mil, respectively.

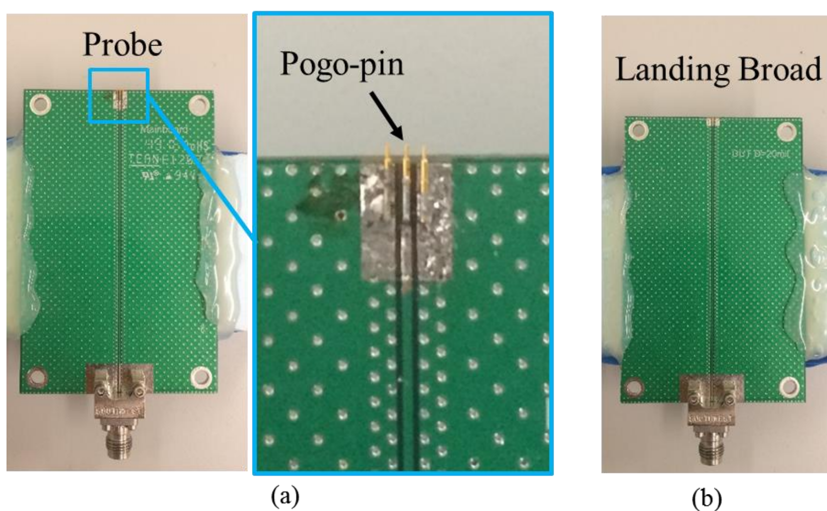

Figure 4 (a) Fabricated Probe and (b) landing board

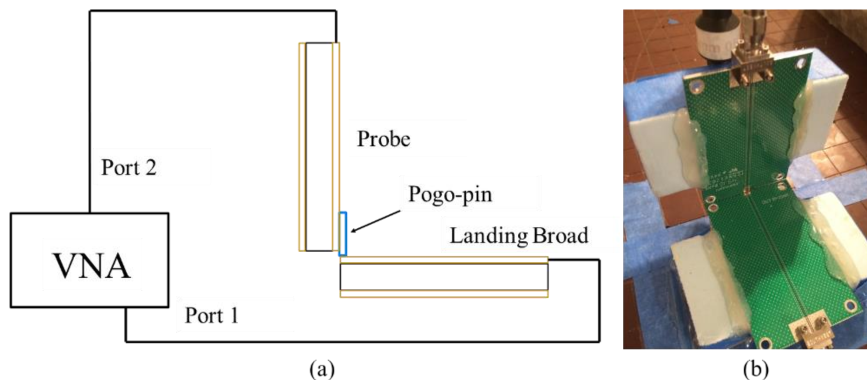

Figure 5 Measurement setup: (a) diagram and (b) actual configuration

To characterize the frequency response of the fabricated probe, the measurement setup described in Figure 5 is used. Port 1 of vector network analyzer (VNA) is connected with the landing board. Port 2 is connected with the probe. The probe is fixed on a robot arm, which is a part of an automatic probing station. The robot arm can be controlled precisely to land the probe on landing board. To make sure the probe landing on the landing pad, the pad position is marked on the top overlay layer.

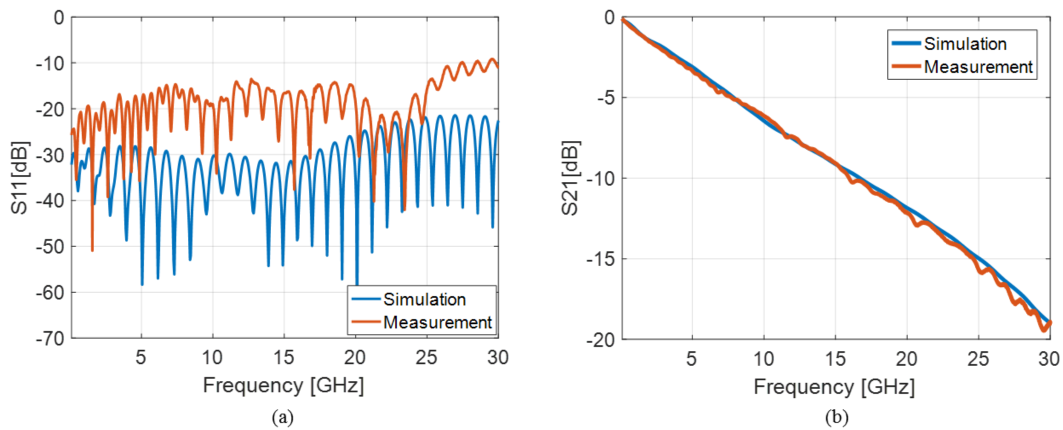

Figure 6 Simulation vs. Measurement results: (a) S11 results (b) S21 results

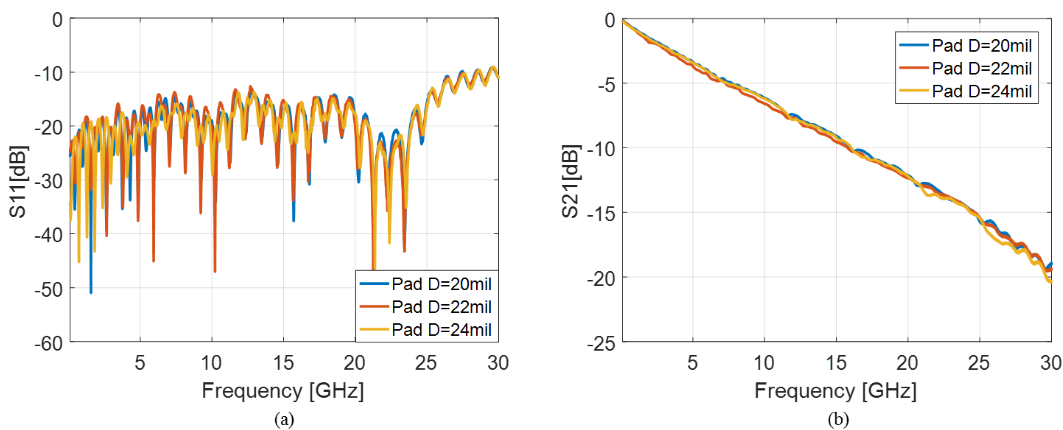

Figure 7 Measurement results with different pad diameters: (a) S11 results (b) S21 results

The simulation vs. measurement results are shown in Figure 6. The measurement S11 results is lower than -13dB when the frequency is below 20GHz. The insertion loss is large, about -12dB at 20GHz. This is due to the lossy material in use and the total length of the channel, around 160 mm. The measured S21 matches well with the simulation result. The measured S11 is about 10dB higher than the simulation result. The difference of S11 between simulation and measurement may be due to manufacturing technology, soldering accuracy and pogo-pin qualities. Since the tiny pogo-pins are soldered manually, the position of a pogo-pin may not be controlled precisely. The difference between simulation and measurement S11 result is acceptable.

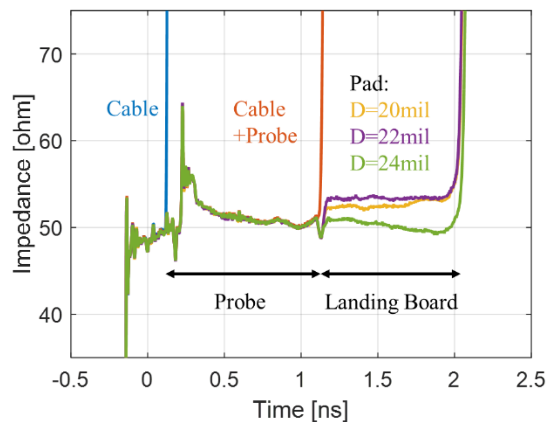

Figure 8 TDR results. The probe is connected with a short cable which is connected to instrument.

To figure out the effect of the landing pad size on S11 and S21 results, landing boards are built with different diameters of landing pad: 20mil, 22mil and 24mil. Figure 7 shows the S11 and S21 results with different diameters. The landing pad is used to compensate the drop of the p.u.l capacitance of the pogo-pins and thus to decrease the discontinuity effect at the transition position. The S21 results of different landing pads are

very close, since the insertion loss is dominated by the CPWG structure. When the frequency goes beyond 25GHz, the S11 and S21 results are much worse no matter which diameter of pad is used. The probe is resonant at high frequencies.

To figure out the characteristic impedance of the transition part, TDR is measured. To distinguish the probe and the landing board on TDR results, cable, cable with probe and cable with probe and landing board are measured separately, as shown in Figure 8. Before the blue curve, it is the TDR results of the cable. Between the blue and the red curve, it is the TDR result of the cable and the designed probe. In TDR measurement, three landing boards with different diameters of landing pad are measured. The TDR result at 1.1ns indicates the transition. The transition works well except there is a small acceptable dip on characteristic impedance. The characteristic impedances of these 3 landing boards are different. The TDR result shows the transition part is not influenced by diameter of the landing pad. Combining with the previous S-parameter results, it shows that the performance of the designed probe is not sensitive to the pad size. This is good for practical usage since the probe doesn’t set up any prerequisite for the DUT. When the probe lands on the DUT, pogo-pins are compressed and impedance discontinuity is further reduced.

4. CONCLUSION

This paper discusses a landing probe that can be used in automatic probing measurements. The probe is based on CPWG structure and pogo-pins are employed to replace the traditional metal tips. A landing board is designed to validate the landing probe and to study the effects of the landing pad size on the transition. The measured S21 correlates well with simulations. TDR measurement results show the transition part works well. The designed probe performs well up to 20 GHz. Besides, the performance of the designed probe is not sensitive to the pad size.

ACKNOWLEDGMENTS

This paper is based upon work supported by the National Science Foundation under Grant No. IIP-1440110.

REFERENCES

[1] X. Guo, et al., "Design methodology for behavioral surface roughness model," *2016 IEEE International Symposium on Electromagnetic Compatibility (EMC)*, Ottawa, ON, 2016, pp. 927-931.

[2] B. Zhao et al., "A novel z-directed embedded component for the reduction of voltage ripple on the power distribution network for PCBs," *2017 IEEE International Symposium on Electromagnetic Compatibility & Signal/Power Integrity (EMCSI)*, Washington, DC, 2017, pp. 225-230.

[3] Y. S. Cao, X. Wang, W. Mai, Y. Wang, et al., "Characterizing EMI radiation physics for edge-and broad-side coupled connectors," in *Proc. IEEE Int. Symp. Electromagn. Compat. Signal Integrity (EMCSI), 2017*, Washington, DC, USA, 2017, pp. 766-771.

[4] Y. S. Cao et al., “EMI Radiation Physics Using Generalized Characteristic Mode (GCM) Analysis with Loss for Practical Structures,” *2017 IEEE 26th Conference on Electrical Performance of Electronic Packaging and Systems (EPEPS)*, pp. 1-3, 2017.

[5] G. Shen et al., "EMI control performance of the absorbing material for application on flexible cables," *2016 IEEE International Symposium on Electromagnetic Compatibility (EMC)*, Ottawa, ON, 2016, pp. 30-35.

[6] Z. Yan, J. Wang, W. Zhang, Y. Wang, and J. Fan, "A Miniature Ultrawideband Electric Field Probe Based on Coax-thru-hole Via Array for Near-Field Measurement," *IEEE Trans. Instrum. Meas.*, vol. 66, no. 10, pp. 2762-2770, Oct. 2017.

[7] G. Shen, S. Yang, J. Sun, S. Xu, D. J. Pommerenke and V. V. Khilkevich, "Maximum Radiated Emissions Evaluation for the Heatsink/IC Structure Using the Measured Near Electrical Field," in *IEEE Transactions on Electromagnetic Compatibility*, vol. 59, no. 5, pp. 1408-1414, Oct. 2017.

[8] Z. Yan, J. Wang, W. Zhang, Y. Wang, and J. Fan, "A Simple Miniature Ultrawideband Magnetic Field Probe Design for Magnetic Near-Field Measurements," *IEEE Trans. Antennas Propag.*, vol. 64, no. 12, pp. 5459-5465, Dec. 2016.

[9] Q. Wang, Y. Gao, J. Fan, J. Drewniak and R. Zai, "Differential probe characterization," *2016 IEEE International Symposium on Electromagnetic Compatibility (EMC)*, Ottawa, ON, 2016, pp. 780-785.

[10] L. Hua et al., "Characterization of PCB dielectric properties using two striplines on the same board," *2014 IEEE International Symposium on Electromagnetic Compatibility (EMC)*, Raleigh, NC, 2014, pp. 809-814.

[11] B. Chen et al., "Analytical and numerical sensitivity analyses of fixtures de-embedding," *2016 IEEE International Symposium on Electromagnetic Compatibility (EMC)*, Ottawa, ON, 2016, pp. 440-444.

[12] H. Barnes, J. Moreira, H. Ossoinig, M. Wollitzer, T. Schmid and Ming Tsai, "Development of a pogo pin assembly and via design for multi-gigabit interfaces on automated test equipment," *2006 Asia-Pacific Microwave Conference, Yokohama*, 2006, pp. 381-384.

[13] [Online].Available:https://www.emulation.com/cgi-cfm/viewpdf.cfm?dwg=skt3548.pdf

[14] [Online].Available:https://www.mill-max.com/assets/pdfs/027.pdf

[15] D. M. Pozar, Microwave Engineering. Hoboken, NJ, USA:Wiley, 2012, pp. 50.

[16] P. F. Freidl, S. Sattler, M. Gadringer, D. Amschl, U. Muhlmann, G. Holweg, and W. Bosch, "Design of PCB RF probe landing pads for measurements up to 90 GHz," *2016 10th European Conference on Antennas and Propagation (EuCAP)*, Davos, 2016, pp. 1-4.

SECTION

7. CONCLUSION

In this topic, spatial resolution of magnetic near-field probe is studied in first part. The traditional definition of spatial resolution cannot reflect spatial resolution of probe properly. Therefore, the impacts of spatial resolution are studied by using analytical and HFSS model of microstrip and probe. Three dimensions of spatial resolution are presented and discussed. When loop surface is parallel with y-z plane and the probe is used to measure Hx field, the spatial resolution is determined by loop height, loop width and thickness of multiple turns in z-axis, y-axis and x-axis directions respectively. A bend microstrip DUT is designed to reflect spatial resolution of probe properly. Then, the effect of spatial resolution is shown in actual board simulation. In second part, a landing probe which can be used in automatic probing measurements is designed. Landing probe is another type of probe and it is generally employed for S-parameter and TDR measurement. The probe is based on CPWG structure and pogo-pins are employed to replace the traditional metal tips. The designed probe performs well up to 20 GHz.

REFERENCES

[1] Y. Zhang, Y. Wang, J. Xu, C. Sui, B. Sen, S. Jin, J. Fan., "Estimating the via-plane capacitance for differential vias with shared-antipad based on analytical equations," *2017 IEEE International Symposium on Electromagnetic Compatibility & Signal/Power Integrity (EMCSI)*, 2017, pp. 272-276.

[2] Y. Chu, S. Wang, J. Xu and D. Fu, "EMI reduction with near field coupling suppression techniques for planar transformers and CM chokes in switching-mode power converters," *2013 IEEE Energy Conversion Congress and Exposition*, Denver, CO, 2013, pp. 3679-3686.

[3] Y. S. Cao, Y. Wang, L. Jiang, A.E. Ruehli, J.L. Drewniak, and J. Fan, "Characterizing EMI Radiation Physics Corresponding to Distributive Geometry Features Using the PEEC Method," in *Proc. IEEE Int. Symp. Electromagn. Compat.*, 2016, Ottawa, ON, 2016, pp. 764-769.

[4] Q. Huang, F. Zhang, T. Enomoto, J. Maeshima, K. Araki and C. Hwang, "Physics-Based Dipole Moment Source Reconstruction for RFI on a Practical Cellphone," in *IEEE Transactions on Electromagnetic Compatibility*, vol. 59, no. 6, pp. 1693-1700, Dec. 2017.

[5] Q. Huang, L. Li, X. Yan, B. Bae, H. Park, C. Hwang and J. Fan, "MoM-Based Ground Current Reconstruction in RFI Application," in *IEEE Transactions on Electromagnetic Compatibility*, vol. 60, no. 4, pp. 1121-1128, Aug. 2018.

[6] Q. Huang, L. Li, X. Yan, B. Bae, H. Park, C. Hwang and J. Fan, "MoM based current reconstruction using near-field scanning," *2017 IEEE International Symposium on Electromagnetic Compatibility & Signal/Power Integrity (EMCSI)*, Washington, DC, 2017, pp. 549-554.

[7] L. Hua et al., "Characterization of PCB dielectric properties using two striplines on the same board," *2014 IEEE International Symposium on Electromagnetic Compatibility (EMC)*, Raleigh, NC, 2014, pp. 809-814.

[8] B. Chen et al., "Analytical and numerical sensitivity analyses of fixtures de-embedding," *2016 IEEE International Symposium on Electromagnetic Compatibility (EMC)*, Ottawa, ON, 2016, pp. 440-444.

[9] H. Chuang et al., "A Magnetic-Field Resonant Probe with Enhanced Sensitivity for RF Interference Applications," in *IEEE Transactions on Electromagnetic Compatibility*, vol. 55, no. 6, pp. 991-998, Dec. 2013.

[10] G. Li, K. Itou, Y. Katou, N. Mukai, D. Pommerenke and J. Fan, "A Resonant E-Field Probe for RFI Measurements," in *IEEE Transactions on Electromagnetic Compatibility*, vol. 56, no. 6, pp. 1719-1722, Dec. 2014.

[11] L. Guan, G. Maghlakelidze, X. Yan, S. Shinde and D. Pommerenke, "Optimizing measurement SNR for weak near-field scanning applications," *2017 IEEE International Symposium on Electromagnetic Compatibility & Signal/Power Integrity (EMCSI)*, Washington, DC, 2017, pp. 687-691.

[12] G. Maghlakelidze et al., "SNR Analysis and Optimization in Near-Field Scanning and EMI Applications," in *IEEE Transactions on Electromagnetic Compatibility*, vol. 60, no. 4, pp. 1087-1094, Aug. 2018.

[13] N. Ando et al., "Miniaturized thin-film magnetic field probe with high spatial resolution for LSI chip measurement," *2004 International Symposium on Electromagnetic Compatibility (IEEE Cat. No.04CH37559)*, Silicon Valley, CA, USA, 2004, pp. 357-362 vol.2.

[14] H. Funato and T. Suga, "Magnetic near-field probe for GHz band and spatial resolution improvement technique," *2006 17th International Zurich Symposium on Electromagnetic Compatibility*, Singapore, 2006, pp. 284-287.

[15] Y. Chou and H. Lu, "Space Difference Magnetic Near-Field Probe With Spatial Resolution Improvement," in *IEEE Transactions on Microwave Theory and Techniques*, vol. 61, no. 12, pp. 4233-4244, Dec. 2013.

[16] Y. Chou and H. Lu, "Magnetic Near-Field Probes With High-Pass and Notch Filters for Electric Field Suppression," in *IEEE Transactions on Microwave Theory and Techniques*, vol. 61, no. 6, pp. 2460-2470, June 2013.

[17] D. Uchida, T. Nagai, Y. Oshima and S. Wakana, "Novel high-spatial resolution probe for electric near-field measurement," *2011 IEEE Radio and Wireless Symposium*, Phoenix, AZ, 2011, pp. 299-302.

[18] Z. Yan, J. Wang, W. Zhang, Y. Wang and J. Fan, "A Miniature Ultrawideband Electric Field Probe Based on Coax-Thru-Hole via Array for Near-Field Measurement," in *IEEE Transactions on Instrumentation and Measurement*, vol. 66, no. 10, pp. 2762-2770, Oct. 2017.

[19] Z. Yan, W. Liu, J. Wang, D. Su, X. Yan and J. Fan, "Noncontact Wideband Current Probes With High Sensitivity and Spatial Resolution for Noise Location on PCB," in *IEEE Transactions on Instrumentation and Measurement*.

[20] J. Zhang, K. W. Kam, J. Min, V. V. Khilkevich, D. Pommerenke and J. Fan, "An Effective Method of Probe Calibration in Phase-Resolved Near-Field Scanning for EMI Application," in *IEEE Transactions on Instrumentation and Measurement*, vol. 62, no. 3, pp. 648-658, March 2013.

VITA

Xin Yan received the B.S. degree in Applied Physics from Beihang University, Beijing, China, in 2015.

He received the Master of Science in Electrical Engineering from Missouri S&T in December 2018.

His research interests included near-field probe development, signal integrity design for High-Speed Printed Circuit Boards and crosstalk analysis.